

Tropical cyclone induced compound flooding in Madagascar: A coupled modeling approach

Md Jamal Uddin Khan¹, Fabien Durand¹, M. Afroosa¹, Paul Coulet¹, Xavier Bertin²,
Valerie Mueller^{3,4}, Yann Krien¹, Caroline Wainwright⁵

¹LEGOS UMR5566, CNRS/CNES/IRD/UPS, Toulouse, France

²LIENSs, UMR7266, CNRS/LRU, La Rochelle, France

³Arizona State University, Tempe, Arizona, USA

⁴International Food Policy Research Institute, Washington, DC, USA

⁵University of Leeds, Leeds, UK

* Corresponding author: Md Jamal Uddin Khan, Email: jamal.khan@univ-tlse3.fr

Keywords: Compound flooding, Madagascar, Cyclone, Batsirai, SCHISM-WWM, SFINCS

Abstract. Compound flooding occurs when multiple contributing factors, such as oceanic (storm surge, tide, and waves) and continental (heavy rainfall and river discharge), combine to exacerbate flood impacts. Tropical cyclone (TC)-induced compound flooding is a major hazard and societal concern, particularly in underdeveloped, highly exposed and vulnerable countries like Madagascar. Despite being repeatedly impacted by TCs, the region receives little attention from the scientific community, particularly in the modeling of TC-induced flooding and associated hazards. Here, we developed a high-resolution (30 m) compound flood model over Madagascar. The model is nested in a regional tide-surge-wave model purpose-built for this region. A dedicated topographic and bathymetric dataset was developed to accurately represent the whole land-ocean continuum. Using this framework, we modeled a recent intense TC Batsirai (2022) and assessed the resulting flooding. Our model shows good accuracy, achieving a hit ratio of 0.83 when matched with the remote sensing derived flood map. Our results demonstrate that the TC-induced flooding in this region is compound in nature, with flooding being significantly underestimated when continental factors (e.g. rainfall-runoff) are excluded. The impact of the ocean is primarily observed along the coastline, extending 5–10 km inland along the rivers. Additionally, we identified a non-linear interaction between oceanic and continental factors, which has important implications for the numerical modeling of such compound flood events. We estimate that at least 30% of the flooded area in our modeled domain comprises agricultural lands, highlighting the potential for significant societal impact. The developments and findings of this study pave the path forward for a national-scale compound flood modeling over Madagascar at a resolution suited for household-scale flood risk and impact assessments.

1 Introduction

Tropical cyclones (TCs) are among the costliest and deadliest of natural disasters (Needham et al. 2015). Each year about a hundred TCs develop over the world's oceans, causing numerous deaths and widespread destruction. TC-induced storm surge has received significant attention in the literature due to its association with nearly one million deaths globally over the past century (Bouwer and Jonkman 2018), particularly in low-lying, TC-prone regions like the Bengal delta (Alam and Dominey-Howes 2014; Khan et al. 2022). A stark reminder of this risk in recent time is Cyclone Nargis that made landfall in Myanmar in 2008 and claimed over 100 thousand lives (Webster 2008). In recent years, advancements in early warning systems have significantly reduced human losses during TCs (Paul 2009; Khan et al. 2021). However, the socio-economic impacts and associated losses related to TCs are increasing (Welker and Faust 2013; Halverson 2018), driven by growing exposed population and assets (Hallegatte et al. 2013) as well as the effects of climate change (Emanuel 2021; Bloemendaal et al. 2022). Among the countries exposed to TC-related hazards, the least developed countries are particularly vulnerable (Dasgupta et al. 2010; Hallegatte et al. 2013). Addressing these vulnerabilities necessitates a better understanding and quantification of the hazards associated with TCs to avoid derail national and global efforts to achieve sustainable development goals.

TCs are naturally a conduit of multiple concurrent hazards (AghaKouchak et al. 2020). In addition to heavy winds that drive storm surges, TCs also bring intense rainfall, which alone can cause significant damage, while also contributing to urban and coastal flooding (Wahl et al. 2015). Over coastal zones, continental runoff and local precipitation from a TC can combine with oceanic storm surge, creating a phenomenon now termed as compound flooding (Zhang et al. 2020b). Compound flooding has only recently gained attention, prompted by unprecedented flooding events like during cyclone Harvey in 2017 (Huang et al. 2021). The frequency of compound flooding events is increasing (Bevacqua et al. 2019; Couasnon et al. 2020) with the increase in heavy precipitation during TCs (Wahl et al. 2015; Pfahl et al. 2017) on the backdrop of a rising sea (Fox-Kemper et al. 2021). Under the current trajectory of the warming climate, more intense and precipitation-laden storms are anticipated (Emanuel 2021; Thackeray et al. 2022). Consequently, in both present and future climates, the role of rainfall and continental processes cannot be overlooked when assessing flooding from TCs around the world (Couasnon et al. 2020; Bevacqua et al. 2020).

Among various parts of the world exposed to TCs, the South-Western Indian Ocean – stretching from Mozambique, through Madagascar and La Réunion island – is one of the most intensely exposed (Nash et al. 2014), yet least studied regions (Needham et al. 2015). On average, 9 TCs develop per year in the South-West Indian Ocean, which amounts to about 14% of the global TCs (Ramsay et al. 2011; Bié and de Camargo 2023). The TCs that have passed by Madagascar over the past two decades are shown in Figure 1 based on best track data from International Best Track Archive for Climate Stewardship (IBTrACS, Knapp et al. 2018). The colorbar in Figure 1 indicates the cyclonic strength, categorized in Saffir-Simpson scale. In total, 75 TCs were identified, which amounts to about 40% of the TCs that developed in South West Indian Ocean. For comparison, on average, 7 TCs develop per year in the North Atlantic, with 2 making landfall in the continental U.S. (Vecchi and Knutson 2011). Many of the TCs that impacted Madagascar made landfall with very high intensity, a recent example being cyclone Batsirai (2022) and cyclone Freddy (2023).

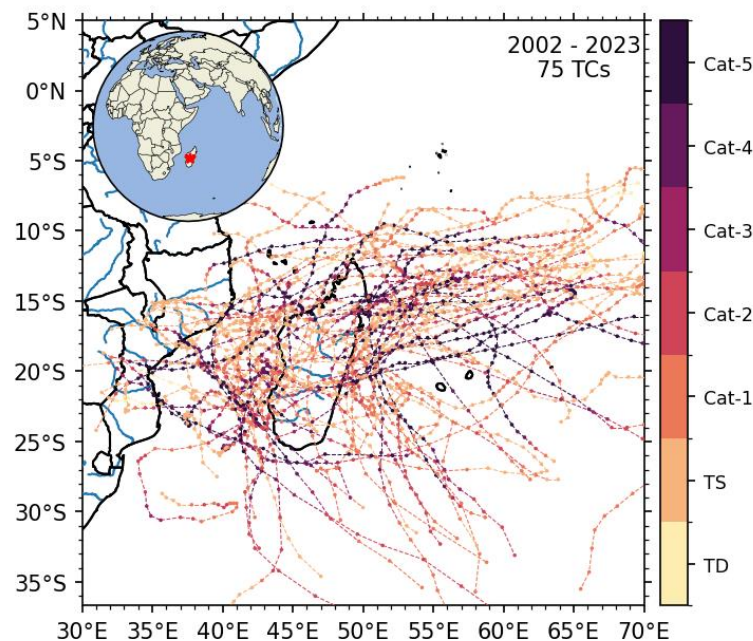


Figure 1. Historic cyclones passing in the vicinity of Madagascar from IBTrACS dataset over 2002-2023 period. Colorbar indicates the cyclonic strength categorized in Saffir-Simpson scale (Cat-1 to Cat-5) as well as Tropical Depression (TD) and Tropical Storm (TS).

The TCs impacting Madagascar develop in the southern Indian Ocean, between Mozambique and Australia. From Figure 1, their tracks can grossly be classified into two main types. Some TCs follow a track that curves southwards after hitting the east coast of Madagascar, impacting only the eastern side of the island (Beucher 2010; Nash et al. 2014). On the other hand, some TCs cross the entire Madagascar landmass before moving into the Mozambique channel and

making landfall again on the east coast of Mozambique (Fitchett and Grab 2014). The mountainous topography of Madagascar essentially acts as a land-shield for many of the intense cyclones that develop in this region, while producing orographic rainfall. In fact, this entire region is home to some of the most precipitation-laden storms (Needham et al. 2015). Despite this, only a handful of regional storm surge modeling studies have been published for the region, mostly covering Mozambique (Bié et al. 2017; Prime 2018) or La Réunion island (Daniel et al. 2009). Moreover, these studies did not address compound flooding from TC-induced precipitation, which can significantly contribute to the flood risk. Overall, Madagascar appears to be a "void" in TC-flooding related research, despite frequently being featured in the news for TC-induced flooding that impacts hundreds of thousands of people (Reuters 2022).

Madagascar is home to approximately 32 million people, with an average population density of 55 people per square kilometer. It is one of the poorest countries globally, with a GDP per capita of only 529 USD in 2023, ranking 188th in the world (IMF 2023). Such low economic wealth significantly increases the country's vulnerability to the impact of TCs (Dasgupta et al. 2010). One notable social impact of TCs in this region is a large-scale human migration in the form of displacement (OCHA 2022a). Quantifying the flooding hazards associated with TCs is crucial for understanding these socio-economic impacts. This requires enhanced monitoring systems and the development of efficient and accurate hydrodynamic modeling frameworks.

Across the global coastline, numerical coastal ocean modeling has been a very potent tool for assessing storm surge hazards (Bertin et al. 2014; Krien et al. 2017b; Bié et al. 2017; Liu et al. 2020; Tran et al. 2024). Improved and efficient coupled ocean-wave model combined with statistical and statistical-deterministic techniques of modeling cyclonic storms allowed development of robust storm surge hazard assessments (Lin et al. 2012; Krien et al. 2017a; Khan et al. 2022). Subsequently, assessment of social vulnerability to coastal storm surges at commune-scale became possible (Bernard et al. 2022). In recent year, further improvement of the modeling of the cyclone induced flooding has emerged by explicitly integrating rainfall and runoff associated with cyclones, conducive to compound flooding (Nederhoff et al. 2024; Green et al. 2025). Our study region, Madagascar, is highly exposed to cyclone as shown in Figure 1. Consequently, the land-ocean continuum of Madagascar is susceptible to heavy rainfall, storm surges, and extreme wave activity. An assessment of the resulting compound flooding hazard requires development of a dedicated land-ocean coupled compound flood modeling framework that integrates all the necessary natural drivers. In addition, further assessment of vulnerability and climate migration related flood within this region requires

high-resolution flood hazard assessment. Achieving such high-resolution compound flood modeling is by itself a challenging task, both technically and numerically (Xu et al. 2022). In addition, a significant obstacle to achieve such modeling is also linked to the lack of geophysical data, a common issue in many underdeveloped regions worldwide.

Recent advances in spaceborne remote sensing have made reasonably accurate geophysical observations more accessible than ever, even in extremely data-scarce regions like Madagascar. The modeling of compound flooding has also progressed substantially, with recent efforts integrating rainfall-runoff processes into 2D hydrodynamic flood modeling frameworks (Huang et al. 2021; Eilander et al. 2023). Leveraging these advancements in numerical modeling and the increasing availability of remote sensing datasets, this study aims to address the critical need for a better understanding of TC-induced compound flooding hazards across Madagascar's land-ocean continuum.

In this paper, we develop a coupled modeling framework to capture the flooding during the recent intense TC named Batsirai that was formed over South-Western Indian Ocean during 2022 and made its landfall in the Mananjary Basin in Madagascar. This cyclone brought intense wind and heavy precipitation, induced widespread coastal and inland flooding, and caused significant casualties and damages. In the present study, we focus particularly on the dynamics of compound flooding, which likely holds the key to explaining observed flooding patterns as well as their associated impacts. To that extent, we first describe the TC Batsirai in Section 2. It is followed by the details of the development of bathymetric data and the atmospheric data processing in Section 3. In Section 4, we describe the oceanic and continental components of our coupled modeling framework. Subsequently, the results are presented and discussed in Section 5 and the paper is concluded in Section 6.

2 TC Batsirai (2022)

Our study focuses on the most-intense recent TC that made landfall in Madagascar in 2022 named TC Batsirai. The track of this TC near Madagascar is depicted in Figure 2. Batsirai was a category-4 equivalent TC in Saffir-Simpson scale with a maximum sustained wind-speed of 230 km/h, and a lowest central pressure of 932hPa. The genesis of Batsirai occurred on January 23, 2022, in the South West Indian Ocean. Initially forming as a tropical depression, it gradually intensified into a category-1 TC by January 26, 2022. The system moved fast towards the west, undergoing several intensifications and weakening cycles until February 1. During

the early hours of February 2, Batsirai underwent rapid intensification from a category-2 to category-4 cyclone with a 28 km wide eye. The peak wind speed occurred around 12:00 UTC as the cyclone was approaching Madagascar. It then continued through another eye-replacement cycle while weakening to a category-3 cyclone followed by another rapid intensification to a category-4 system with an estimated central pressure of 934 hPa. TC Batsirai made landfall in Madagascar on February 5 around 18:00 UTC, as a category-3 cyclone, before weakening due to land interaction. While crossing over the Mananjary Basin, TC Batsirai poured a basin average precipitation of about 300 mm in a day (Figure 2b). Such heavy precipitation is bound to cause sharp rise in the rivers located along this coast (Aldegheri 1972). The heaviest precipitation occurred on the southern flank of the cyclone track (Figure 2b, inset), which also corresponds to the region experiencing the maximum wind speed. After crossing Madagascar as a remnant system, TC Batsirai regained strength over the Mozambique channel, eventually transitioning into an extra-tropical cyclone before dissipating as it moved southward.

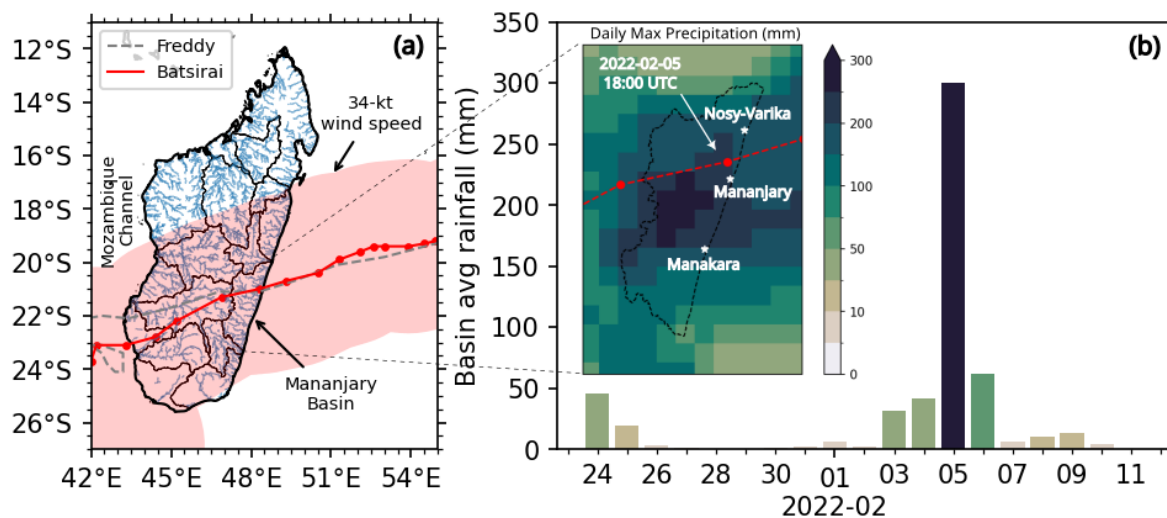


Figure 2. (a) Basins of Madagascar based on HydroBASINS (Lehner and Grill 2013). Red line shows the track of TC Batsirai (2022) passing through Madagascar over Mananjary basin. The impacted zone delineated from the 34-kt wind speed extent is shaded. The same location was also impacted by TC Freddy in 2023. (b) Daily rainfall averaged over Mananjary basin. Inset shows the maximum daily precipitation amount over the region during TC Batsirai. The Mananjary basin outline is shown by a black dashed line and the location of Nosy-Varika, Mananjary, and Manakara is shown with white stars.

Cyclone Batsirai was reported to cause massive destruction along its path, with significant flooding in Nosy-Varika, Mananjary, and Manakara (OCHA 2022a; WMO 2022). The cyclone claimed at least 123 lives (OCHA 2022b), and resulted in economic losses exceeding 190 million USD across Madagascar, La Réunion, Mauritius (AON 2022). In Madagascar, the

agricultural loss was estimated to be about 47 million euros, or about 53 million USD (Le Quotidien 2022). Grossly, the economic damage amounts to 1% of gross domestic product (GDP) of Madagascar. The devastation from cyclone Batsirai in Madagascar included the destruction of over 19 thousand houses – 9,000 destroyed, 3,000 damaged, and 7,000 flooded. Additionally, more than 4,000 classrooms were affected, severely disrupting education and shelters (OCHA 2022b). In an estimate across hundreds of sites, cyclone Batsirai displaced over 60 thousand people (OCHA 2022a).

3 Data

Numerical modeling of compound flooding requires various datasets, including topography, bathymetry, river hydrography, land-use/land-cover, and various environmental forcing fields. Among these datasets, we have put particular attention towards the bathymetry and topography, which is the main geometric factor that dictates not only the flow characteristics but also flooding. This is also often the main factor that influences model quality (Krien et al. 2016). In addition, we have applied bias corrections and data fusion to accurately represent the environmental forcing in the models. These two are discussed in details in this section. Other datasets that have been used in model development, or in validation are presented as we utilize them.

3.1 Bathymetry and topography

High-resolution and accurate bathymetry and topography is one of the main requirements for any successful flood modeling effort. However, acquiring a reliable and high-resolution bathymetric and topographic dataset is one of the most challenging aspects of such modeling. We have used a combination of remote sensing-derived and in situ datasets which are described below.

3.1.1 Chart dataset

The first source of bathymetric data comes from a set of digitized navigational charts published by the French national hydrographic service (Shom, <https://diffusion.shom.fr/cartes/cartes-marines.html>). We have acquired and digitized two charts in the framework of this paper (See Figure S1 in the supplementary materials). Chart 6672 covers the whole Madagascar island at 1:3500000 scale, and chart FR274890 covers the part of our study domain at a finer scale. Chart 6672 is a paper chart, which was digitized by hand amounting to about 19 thousand sounding points. On the other hand, chart FR274890 is a vector chart that was converted to sounding

points through Geographic Information System (GIS) toolbox (python shapely, <https://shapely.readthedocs.io/>) resulting in about 31,000 points. The chart data is provided in so-called Chart Datum (CD). Using the global tidal model FES2014 (Lyard et al. 2021), we have vertically referenced it to the Mean Sea Level (MSL) (Simon 2013; Fuchs et al. 2021). The chart resolution varies from relatively close soundings and contours (10, 30, 50m) at the coastline, with sparse data for much deeper regions. For the domain of the continental model, that only covers a small part of the nearshore ocean, chart data sufficiently cover the whole oceanic part of the model domain. Indeed, if available, Shom charts of similar resolution as FR274890 covering the whole ocean model domain would have been ideal. In the absence of such dataset at the current moment, the remaining parts of the ocean model domain were supplemented from the global GEBCO dataset (v2022, <https://gebco.net>, last accessed: 22/06/2022).

3.1.2 FABDEM

The land topography of the modeled region is obtained from the FABDEM dataset (Hawker et al. 2022). This 30 m resolution topographic dataset is vertically referenced to the geoid (EGM2008). The dataset is built on top of the Copernicus 30 m digital terrain model (DTM), where the vegetation and the other settlement features are removed using a machine learning technique (Hawker et al. 2022). This dataset has been extensively validated in challenging environments (Seeger et al. 2023) and has been extensively used in compound flood modeling in recent years (Eilander et al. 2023; Olcese et al. 2024; Wing et al. 2024). However, this topography dataset does not contain any ocean depth information (set to 0). As our ocean circulation model is referenced to the mean sea level (MSL), to ensure the datum continuity, we have used the Mean Dynamic Topography by CNES/CLS (Mulet et al. 2021) derived from altimetry to transfer the datum from geoid to mean sea level.

3.1.3 Intertidal DEM (*pyIntertidalDEM*)

At the very interface of the land and ocean lies the inter-tidal zone, where the bathymetric coverage is typically the poorest and often erroneous (Mason et al. 2000; Krien et al. 2016). The topographic data (e.g., FABDEM) is derived from relatively older X-Band radar dataset. The coast of Madagascar experiences frequent energetic wave conditions (Reguero et al. 2012; Gaffet et al. 2024), tide (Lyard et al. 2021), and large sediment supply particularly in the west coast (Brooke et al. 2020). These factors drive continuous change in the inter-tidal topography. Additionally, as mentioned previously, the topography data do not cover the water depths of

the ocean. A similar issue of changing shoreline also affects the charts dataset. Moreover, the sampling done by the hydrographic agencies near the coast (very shallow water) is typically minimal due to limited access by boat, and often reporting shallower levels to ensure safer navigation (Simon 2013). For our study region, where the beach shoreline extent is quite narrow with nearby settlements, it is thus imperative to properly resolve this inter-tidal area. To do that, we have used the pyIntertidalDEM method – an in-house toolbox to extract the inter-tidal topography from high-resolution Sentinel-2 imagery at 10 m resolution (Khan et al. 2019). A total 242 images over 53 tiles (1° by 1°) were analyzed and referenced vertically with our ocean circulation model (See Numerical models). Hence, by construction, the vertical datum for this data is MSL. Since it is an inter-tidal topography, it covers the land band located between the FABDEM topography and chart bathymetry dataset, thus ensuring an accurate representation of the shoreline and a smooth transition between the land and the ocean.

3.1.4 Hydrography and river

The above-described bathymetry and topography datasets, while providing a reasonable description of the geometry of our modeling domain, do not resolve the rivers' depths properly. To circumvent this issue, additional river hydrography data is obtained from (Lin et al. 2019). They provide a global estimate of the bankfull river discharge (1-in-2-year simulated return value) and the river width. We have clipped this dataset over our region of interest and applied minor corrections to the rivers to properly intersect the coastlines. Based on the bankfull discharge and river width, a rectangular channel depth is estimated using a power law relationship $h = aQ^b$. A default value of 0.27 and 0.30 for the parameters a and b are used based on Andreadis et al. (2013), and a minimum river depth of 0.5 m is imposed. The river-bed elevation is then estimated by reducing the existing bed level by bankfull depth and burned onto the bathymetry-topography data described above. This resulted in a more realistic representation of the river hydrography in the final topography bathymetry dataset used for numerical modeling over the continent.

3.2 Atmospheric forcing

For our numerical hydrodynamic modeling, we need several atmospheric forcing fields. These include wind speed at 10m MSL level, pressure reduced to MSL, and precipitation. The bulk of these data is obtained from the European Center for Medium-Range Weather Forecasts (ECMWF) reanalysis version 5 (ERA5) (Hersbach et al. 2018, 2020). With a 12-hour assimilation window, ERA5 ensures a smooth hourly product, which is chosen for the present

study. It has been used globally for various relevant modeling activities, including storm surge (Muis et al. 2020; Mentaschi et al. 2023), wave-climate (Gaffet et al. 2024), and hydrology (Harrigan et al. 2020). However, the extreme events, which are the focus of our study are typically underestimated in ERA5 (Mazza and Chen 2023; Kumar et al. 2024; Gaffet et al. 2024). We have applied data fusion and bias correction to circumvent various underestimations as discussed below.

3.2.1 Wind and pressure

We have extracted zonal and meridional wind speed at 10m height and at a 25 km remapped resolution from Copernicus Climate Service portal (Hersbach et al. 2018). We have applied the bias correction on the total wind speed according to Gaffet et al. (2024). Furthermore, we have also obtained the cyclones best track dataset from Joint Typhoon Warning Center (JTWC). This dataset of every storm contains the center of storm, central pressure, maximum wind speed, and when available the 34, 50, and 64-knots wind radii along the trajectory of the storm. Wind speed is derived using this dataset from analytical formulation of Emanuel and Rotunno (2011) for the inner-core and using Holland (1980) formulation for the outer core as suggested by Krien et al. (2018). On the other hand, the analytical pressure field is derived using the Holland (1980) formulation. Available radial distance information is used to better constrain the computation of radius of maximum winds (R_{max}) in the analytical model (Krien et al. 2017b; Khan et al. 2021). Use of such analytical wind and pressure field is well known in storm surge modeling (Lin and Chavas 2012) and has been extensively used in previous studies (Krien et al. 2017a; Khan et al. 2022).

The analytical wind and pressure field is derived on a higher-resolution 0.025° grid that better corresponds the high-resolution coastal models. The bias corrected ERA5 data is up-sampled linearly and merged with the analytical wind and pressure fields based on the distance from the center of the storm similar to Khan et al. (2021). Only analytical fields are used from the center of the storm to 3 times the R_{max} . Outside of 10 times the R_{max} , only ERA5 data is retained. In between, the sources are fused with gradual transitions from analytical fields to ERA5 (Khan et al. 2021).

3.2.2 Rainfall

Similar to wind and pressure, hourly total rainfall is extracted at a 25 km remapped resolution from Copernicus Climate Service portal (Hersbach et al. 2018). We refrained from using remote sensing derived products, such as GPM/TRMM. It is because along the eastern side of

Madagascar, the pattern of annual rainfall observed by GPM/TRMM appears to be spatially shifted eastward relative to a reference in situ derived annual rainfall dataset (Rija 2019), as shown by (Leroux et al. 2023, 2024). Consequently, the inland rainfall estimates from GPM/TRMM is underestimated (Szabó et al. 2015; Leroux et al. 2024). Interestingly ERA5 does not show such spatial bias which is potentially due to some data assimilation (Leroux et al. 2023, 2024).

Similar to wind and pressure fields, the precipitation rate is also underestimated in ERA5 (Hersbach et al. 2020). Such underestimation is more pronounced during extreme events such as storms (Kumar et al. 2024), and tropical cyclones (Mazza and Chen 2023), which is the focus of our study. Over the continental United States, Mazza and Chen (2023) compared the ERA5 rainfall with radar-derived rainfall and found that ERA5 underestimates the rainfall during tropical cyclone events by a factor of 2 across all quantiles. For our study over Madagascar, we thus tested two versions of the ERA5 rainfall dataset. One is without applying any correction (identified simply as ERA5). On the other hand, is ERA5x2, where the ERA5 rainfall was multiplied by a factor of 2 across all quantiles, as estimated by Mazza and Chen (2023). This literature-based bias correction is considered a first-order estimate of precipitation bias over Madagascar in the absence of regional studies or observed data for a regional bias analysis.

3.3 Auxiliary datasets

In addition to the bathymetry and topography dataset in Section 3.1, atmospheric forcing datasets described in Section 3.2, we also resorted to several auxiliary datasets to derive the necessary inputs to the model. These datasets include the global curve number dataset GCN250 at 250 m resolution (Jaafar et al. 2019), a Hierarchical Ensemble Model estimates of soil water retention (soil effective porosity) at 0.083° resolution (Zhang et al. 2020a), and a remote-sensing derived land-use land-cover (LULC) dataset from Copernicus at 100 m resolution (Buchhorn et al. 2020a). The use of these datasets and necessary additional details are provided wherever they are used in the subsequent sections.

A brief summary of the datasets indicating resolution, strengths, and weaknesses is presented in Table 1.

335 Table 1. Summary of the datasets used for model development.

Dataset	Variable (s)	Resolution	Strength	Weakness
Chart (Shom)	Sounding depth	Variable	More accurate	Non-uniform Not public Limited coverage
FABDEM (Hawker et al. 2022)	Topographic height	30m	Global dataset	Misrepresented river depths No referenced to MSL
pyIntertidalDEM (Khan et al. 2019)	Topographic height	10m	Remote sensing derived	Depends on the availability of absolute local water level records for vertical referencing
River hydrography (Lin et al. 2019)	River width Bankfull discharge	NA	Global	Only 1-in-2 year bankfull discharge
CNES-CLS18 (Mulet et al. 2021)	Mean dynamic topography (m)	0.125°	Altimetry derived	No estuarine coverage Potentially erroneous close to the coast
ERA5 (Hersbach et al. 2020)	Wind speed Pressure Total Precipitation	0.25°	Global	Extremes are underestimated
GCN250 (Jaafar et al. 2019)	Curve number	250m	Global	Propagated errors associated with LULC and Hydrologic soil group
Zhang et al. (2020a)	Soil effective porosity	0.083°	Global, Ensemble dataset	Non-uniform and sparse validation samples
Copernicus LULC (Buchhorn et al. 2020a)	Land-use Land-cover classes	100m	Global	Classifications not locally adapted Without seasonality

336 **4 Numerical Models**

337 Our objective in this paper is to study the compound flooding in Madagascar, which occurs
338 due to both oceanic and continental factors. Many previous studies have relied on readily
339 available storm-surge estimates from global models, such as GTSM (Muis et al. 2020) to
340 simply drive local compound flood models. However, such datasets are derived from models
341 forced with global atmospheric datasets, which often underestimate extreme winds, pressure
342 drops (Krien et al. 2017b; Khan et al. 2021; Gaffet et al. 2024) and rainfalls (Mazza and Chen
343 2023). In addition, the resolution can be coarse (e.g., maximum 2.5 km in GTSM), which is

not enough to resolve the fine-scale coastal dynamics, such as tide-surge interactions and wave setup, properly (Bertin et al. 2014). More importantly, these global models rely on global bathymetric datasets, which often contain large biases, particularly in data-poor and shallow areas (Krien et al. 2016), such as the coastal oceans of Madagascar. Hence, we developed our dedicated modeling platform that covers from the deep ocean to the continental hydrology based on the custom-made topographic-bathymetric dataset described in Section 3.1. Beyond the benefit of the bathymetry-topography and the modeling resolution, this dedicated modeling framework also allows us to assess the sensitivity to the atmospheric forcing fluxes used, as well as to correct their biases when necessary.

Our modeling framework has two main components. For modeling the ocean circulation and storm surges we have used a coupled SCHISM-WWM model (Roland et al. 2012; Zhang et al. 2016) that covers the seas around Madagascar. On the other hand, for modeling the coast-to-inland of our study region in Madagascar, we have adopted a reduced physics compound flood model called SFINCS (Leijnse et al. 2021; Van Ormondt et al. 2025). It is noteworthy here that SCHISM has already been applied to compound flood modeling in stand-alone mode (viz. without resorting to any other model for the continental part of the domain), with success (Huang et al. 2021, 2023). In our application over Madagascar however, we only use SCHISM-WWM for the oceanic part of the domain without considering it for the compound flood modeling. The primary constraint that drove our choice was the computational requirements. The larger objective of our work is to develop flood hazard assessments for an interdisciplinary study of the impact of environmental hazards on the Malagasi society, economy, and internal migration. This demands very fine-scale assessment of flooding hazard, preferably at the household scales (typically in the order of 10 m). A cross-scale standalone SCHISM-WWM configuration covering the whole Madagascar domain at a sufficiently high resolution would be too costly, as suggested by the nation-scale application developed over Japan (Huang et al. 2023). The development of the SCHISM model over continental regions for compound flooding applications is also relatively delicate since extensive high-resolution topography dataset is necessary to appropriately resolve the various geometric structures (Zhang et al. 2020b; Huang et al. 2021, 2022). In comparison, SFINCS model solves simplified flow equations on a structured grid, hence the model development is relatively straightforward and the computations are much cheaper. Additionally, the hydrologic features (e.g., various rainfall-runoff models, soil filtration) are not currently built in SCHISM-WWM. Hence, it requires implementation of pre-computed water fluxes across the model domain (Huang et al.

2023). Such functionalities already built-in inside SFINCS pleaded for considering the SCHISM-SFINCS coupling strategy used in the present study.

The model domains are illustrated in Figure 3. In the next subsections we describe these two models and the one-way coupling between them used in the present study. We deliberately put more emphasis on the details of our compound flood model (SFINCS) as its results will be the main focus of this paper.

4.1 Coupled ocean-wave model (SCHISM-WWM)

To model the oceanic factors for our compound flood modeling, we have developed a regional ocean circulation model based on open-source code SCHISM (Zhang and Baptista 2008; Zhang et al. 2016). SCHISM is a cross-scale 2D/3D hydrodynamic model that solves the primitive equations on an unstructured mesh of varying resolution. SCHISM uses a semi-implicit time-stepping scheme combined with an Eulerian-Lagrangian method for advection. Such numerical method allows very efficient computation with highly variable mesh resolution, typical of cross-scale applications (Zhang et al. 2016; Khan et al. 2021). SCHISM also includes a wetting-and-drying scheme, which is instrumental for proper modeling of the coastal flooding. SCHISM has previously been applied at local to global scales for modeling tide (Krien et al. 2016; Zhang et al. 2023), storm surges and associated coastal flooding (Bertin et al. 2014; Krien et al. 2017b; Khan et al. 2021; Mentaschi et al. 2023).

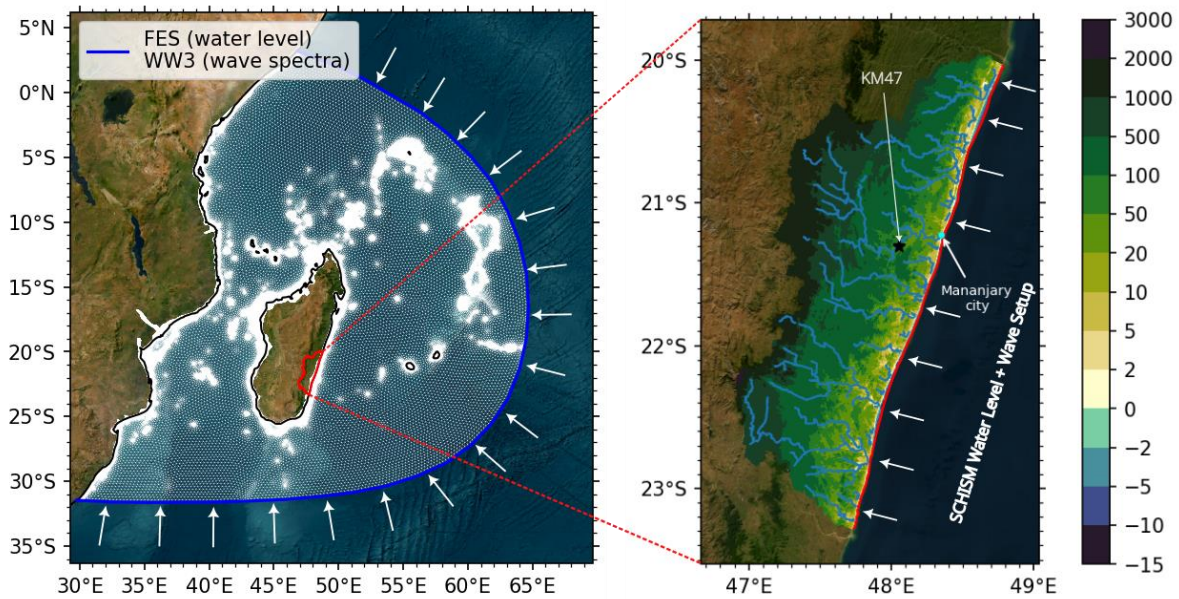


Figure 3. Larger scale wave-coupled ocean circulation model SCHISM+WWM (left). Blue line shows the imposed model boundary, where tidal forcing originates from the global FES 2014 tidal model and the sea states from a regional application of the WaveWatchIII model. The outline of SFINCS continental flood model is shown in red and in detail on the right. Black star indicates the only altimetry virtual station in this basin. The location of Mananjary City is shown in cyan dot.

In our application over Madagascar, SCHISM is coupled with WWM, a third-generation spectral wave model, allowing for representing the effects of short waves on the mean hydrodynamic circulation, including the development of a wave setup along the coast. This coupled oceanic model is henceforth termed as SCHISM-WWM in the rest of this manuscript.

The overall model domain of SCHISM-WWM over Madagascar (Figure 3) covers from 30°E to 64°E and 32°S to 4°N. The model domain is extended up to 20 m above MSL inside Madagascar and up to 10 m above MSL along the eastern shoreline of Mozambique. The computational mesh is made of triangular elements. It is based on the topographic-bathymetric dataset described before (excluding river hydrography). The mesh resolution is finer wherever the bathymetry is shallow or steep, similar to Krien et al. (2016). The coarsest resolution is 30 km, typically in the deepest parts of the domain in the offshore ocean. Along the Madagascar coastline, the finest resolution is 500 m. On the other hand, along the coastline of Mozambique, the resolution is 1000 m. Overall, the model mesh amounts to around 500 thousand nodes and around 1 million elements.

We have adopted a depth-average formulation for our modeling over Madagascar similar to Khan et al. (2021). The bottom friction is modeled with a regionally constant Manning's coefficient of 0.04. This value is albeit a bit larger than the typical value (0.025) (Bunya et al.

2010), but it has been tuned to produce the best comparison with the observed tidal characteristics (see supplementary materials). Here, the most appropriate model time step was found to be 600 s, which is typical of applications with similar spatial resolutions (Fassoni-Andrade et al. 2023). Additional details regarding the ocean model validation is provided in the supplementary materials. For all simulations, the model is forced at its oceanic open boundaries with water levels from FES2014 global tidal atlas (Lyard et al. 2021).

The wave model WWM is coupled with SCHISM at source-code level and shares the same model grid and domain decomposition (Roland et al. 2012). We consider all the relevant source terms including wave growth and energy dissipation due to white-capping (Bidlot et al. 2007; Bidlot 2012), deep (Hasselmann et al. 1985) and shallow water (Eldeberky 1996) non-linear interaction, effect of bottom friction (Hasselmann et al. 1973), and wave breaking (Battjes and Janssen 1978) using the adaptive parameterization of (Pezerat et al. 2021). Every 30 minutes, SCHISM passes the wind forcing and water level to WWM. Wave radiation stresses as well as friction velocities are then updated from WWM and passed to SCHISM. Wave spectrum in WWM is discretized in 36 directional bins (0-360°) and 24 frequency bins (0.04-1Hz). Advection in spectral and spatial space is computed using fully implicit schemes.

For the simulations with atmospheric forcing, the custom wind field derived using the combination of analytical field of Emanuel and Rotunno (2011) and Holland (1980) is superimposed on the bias corrected ERA5 (Gaffet et al. 2024) (see Data). Similarly, for the pressure fields, the analytical fields derived from Holland (1980) is superimposed over ERA5. The water level along the boundary is also corrected for the inverse barometer effect.

Particularly for cyclonic events, an additional wave boundary condition is applied to account for the swell that travels from outside of the SCHISM-WWM domain. To do that a regional WaveWatchIII (WW3DG 2019) configuration similar to the one used in Khan et al. (2021) is used here that covers the whole Indian Ocean at a resolution of 0.5°. Here, this model is also forced with the bias-corrected ERA5 wind.

4.2 Compound flood model (SFINCS)

To model the coastal flooding from the coast to top of the river basin, we adopted SFINCS (Super-Fast INundation of CoastS) - a reduced complexity compound flood model (Leijnse et al. 2021). The model domain of SFINCS is shown in Figure 3. Since we will be mainly presenting the results of SFINCS, the formulation and characteristics of this model is further discussed in the following subsections.

4.2.1 Model formulation

SFINCS solves simplified and de-coupled shallow-water equations on a regular, staggered Arakawa-C grid. Bathymetry and water level in this model are defined at the center of each cell, and the flow variables are defined at the face of the cells. The governing equations of SFINCS are based on Linear Inertial Equations (LIE) derived by Bates et al. (2010) with additional advection terms (Leijnse et al. 2021). In this formulation, the volumetric flow rate per unit width (q) at the interface of the cell reads as in Eqn. 1 –

$$q_i^{t+\Delta t} = \frac{q_i^t - \left(gh_i \frac{\Delta\zeta}{\Delta x} + F\right) \Delta t}{1 + \frac{g\Delta t n^2 |q_i^t|}{h_i^{\frac{7}{3}}}} \quad (1)$$

Here, q_i^t is the flow rate with h_i water depth and $\Delta\zeta/\Delta x$ water level gradient at the i^{th} cell interface. Δt is the time step. g and n are the gravitational acceleration and the Manning's roughness coefficient respectively. The water depth at the cell interface h_i is the difference between the maximum water level and the maximum bed levels of two adjacent cells.

F in Eqn. 1 contains the advection and the wind-stress terms. The advection terms in 1-D conservative form are written as Eqn. 2 –

$$\frac{\partial}{\partial x} \frac{q^2}{h} + \frac{\partial}{\partial y} \frac{q_x q_y}{h} \quad (2)$$

Inside SFINCS, the gradients in the advection terms are implemented using an upwind discretization for the model's x-direction and using central difference in the y-direction (Leijnse et al. 2021). Finally, in the original LIE, the water level is computed from the mass-continuity equation (Bates et al. 2010; Leijnse et al. 2021). In our application for Mananjary region of Madagascar, we have adopted the recently developed subgrid version of these equations, where the representative values for the conveyance depth h_i and the Manning's coefficient n are adjusted based on a finer topographic and bathymetric dataset (Van Ormondt et al. 2025). This amounts an up-scaling technique where the flow variables - namely the conveyance depth h_i and the Manning's roughness n in Eqn. 1 are corrected for the finer scale subgrid features (Kennedy et al. 2019). The benefit of this approach is that it allows solving

the LIE in a relatively coarse resolution while retaining the properties of the high-resolution geometry of the topography.

The LIE in subgrid form is defined as Eqn. 3 –

$$\langle q_i \rangle_w^{t+\Delta t} = \frac{\langle q_i \rangle_w^t - (g \langle H_i \rangle \frac{\Delta \zeta}{\Delta x} + F) \Delta t}{1 + g \Delta t n_{i,w}^2 |\langle q_i \rangle_w^t| / \langle H_i \rangle_w^{7/3}} \quad (3)$$

Here, $\langle q_i \rangle_w$ and $\langle H_i \rangle_w$ are average unit discharge and water depth. Subscript w donates the wet average quantity of these variables defined as $\langle Q \rangle_w = \frac{1}{A_w} \iint_{A_w} Q \, dA$ for any quantity Q with corresponding wet area A_w . The wet average area is defined in terms of cell area A as $A_w = \phi A$, where ϕ is the wet fraction. Subsequently, for any hydrodynamic quantity Q , the grid scale quantity $\langle Q \rangle$ amounts to $\langle Q \rangle_g = \phi \langle Q \rangle_w = \frac{1}{A} \iint_{A_w} Q \, dA$.

$n_{i,w}$ is the Manning's n coefficient adjusted for subgrid variation, which is derived by considering Manning's equation for open channel flow. The expression turns out to be Eqn. 4 –

$$n_{i,w} = \frac{\langle H_i \rangle_w^{5/3}}{\langle \frac{H_i}{n} \rangle_w} \quad (4)$$

where the denominator is computed from the subgrid consist of N pixels, with its own bed level $z_{b,k}$ and Manning coefficient n_k . For a water level ζ_i , the water depth in each subgrid pixel is $h_k = \max(\zeta_i - z_{b,k}, 0)$ and the denominator is $\frac{1}{\phi N} \sum_{k=1}^N \frac{h_k^{5/3}}{n_k}$.

In SFINCS, Eqn. 3 is expressed in grid-averaged quantities ($\langle Q \rangle_g$) instead of wet-average quantities ($\langle Q \rangle_w$). For a given subgrid topography and a set of water level, the grid-averaged water depth $\langle H_i \rangle_g$, and associated subgrid Manning and wet fraction ϕ can be stored in a look-up table as a function of water level in a pre-processing step. During simulation, the necessary variable can be easily looked up with interpolation without recomputing in each time step. The number of discrete vertical levels is a user-defined parameter, and 20 levels are shown to be sufficient for an accurate description of the subgrid quantities (Van Ormondt et al. 2025).

In subgrid form, the continuity equation is written as grid-averaged fluxes instead of water level as the corresponding water level is obtained again from a pre-processed subgrid table. The water volume V in a cell is computed as Eqn. 5 –

$$V_{m,n}^{t+\Delta t} = V_{m,n}^t + \left((\langle q_x \rangle_{g:m-1,n}^t - \langle q_x \rangle_{g:m,n}^t) \Delta y + (\langle q_y \rangle_{g:m,n-1}^t - \langle q_y \rangle_{g:m,n}^t) \Delta x + S_{m,n} \right) * \Delta t \quad (5)$$

where, m and n is the cell number in x and y direction, and $S_{m,n}$ is the sources (e.g., inflow, rainfall) and sinks (e.g., infiltration). The g prefix indicates the grid-average fluxes.

In the subgrid table, the wet volume as function of the local water level (ζ) is determined from Eqn. 6 –

$$V(\zeta) = \frac{\Delta x \Delta y}{N} \sum_{k=1}^N m \, ax(\zeta - z_k, 0) \quad (6)$$

In practice, instead of an equi-distance water levels, equi-distance volume levels are defined, which allows for a faster interpolation. During the simulation, the corresponding water level is computed by interpolating over the subgrid table of volume and water level. Further details of the numerical implementation of the subgrid method can be found in Van Ormondt et al. (2025).

Finally, an important assumption of this subgrid approach is that the water level within a cell remains uniform, therefore equal for all subgrid pixels. In practice, such assumption may manifest itself as water level discontinuities in case of complicated subgrid structures.

4.2.2 Rainfall-runoff process

One of the important aspects of compound flood modeling is the rainfall-runoff process. As rain falls, some part of it is "lost" due to canopy storage, evaporation, transpiration, absorption, surface storage. The rest of the precipitation then turns into runoff. Thus, runoff generation depends on many factors such as the land-use/land-cover, soil-structure, antecedent moisture condition, and atmospheric condition. If the sum of rainfall and loss becomes less than or equal to zero, there is no runoff.

The simplest method in SFINCS is to convert rainfall flux to runoff amount by applying a constant infiltration (e.g., constant sink). Such approach is very crude and might only be useful for short simulations over a small region. However, our model domain is relatively large and inhomogeneous which requires a more realistic loss and runoff estimation method. Here we use the Soil Conservation Service (SCS) curve number (CN) method (Ponce and Hawkins 1996; Mishra and Singh 2003). The CN method is designed to compute the runoff amount based on soil properties and antecedent moisture condition. All the loss (e.g., storage, infiltration, evaporation, and transpiration) is computed as a bulk estimate. This empirical method is developed by SCS, and has been extensively used in hydrologic modeling (Mishra and Singh 2003).

In the original curve number method (termed here as CN-A), the runoff R is computed as in Eqn. 7 –

$$R = \frac{(P - I_a)^2}{(P - I_a) + S} \quad (7)$$

where, R and P is the runoff and precipitation amount in inches respectively. S is the soil's moisture storage capacity in inches, which is computed from the curve number (CN) as $S = \frac{1000}{CN} - 10$. Thus, a CN value of 100 means there is no retention in the soil. Typically, the CN value does not go below 40. The initial abstraction (I_a) is estimated as 20% of S .

The original curve number method was developed for a single rain event, with a specified S . Hence, for continuous simulation, the CN-A method cannot be used directly where the effective storage capacity should also evolve over time. This is achieved by assuming that all the losses are transformed into infiltration, and using the infiltration rate to update effective S at each time step. When there is no rainfall, no water infiltrates, and the soil recovers its retention capacity at a given rate, known as the recovery constant K_r (hr^{-1}). K_r is related to the hydraulic conductivity of the soil K_s as $K_r = \frac{\sqrt{K_s}}{75}$ (Rossman and Huber 2016). This modified curve number method is termed here as CN-B. The aforementioned CN methods are implemented in SFINCS and tested on watersheds along the east coast of the USA (Nederhoff et al. 2024).

We have tested both infiltration methods in this study. For CN-A method, we have used the GCN250 global curve number with average antecedent moisture condition (Jaafar et al. 2019). This 250 m resolution dataset is interpolated to our model grid with a nearest neighbor

interpolation. For CN-B method, the curve number is replaced with two input datasets - 1) maximum soil-moisture capacity S_{max} in meters and 2) hydraulic conductivity, K_s in mm/hour. S_{max} is computed using the abovementioned curve number derived by Jaafar et al. (2019). K_s is computed based on the pedotransfer function proposed by Ahuja et al. (1989) as $K_s(cm/hour) = 764.5\phi_e^{3.288}$ (Zhang and Schaap 2019). Soil effective porosity (ϕ_e , also known as saturated moisture content) is obtained from the ensemble mean dataset developed by Zhang et al. (2020a).

4.2.3 Model grid and domain

Cyclone Batsirai (2022) made its landfall in the Mananjary Basin (Figure 2), hence our region of interest for the compound flood model SFINCS. This is the same location where cyclone Freddy (2023) made landfall too. We have defined the model domain using the basin outline obtained from the HydroBASINS dataset at level 5 (Lehner and Grill 2013). All the individual basins over Madagascar are shown in Figure 2a. For the current study, we develop our SFINCS model only over the Mananjary Basin.

The area of Mananjary Basin obtained from HydroBASIN dataset is extended towards the ocean, where the model is forced with the SCHISM-WWM water level. The one-way coupling is described in detail in the next section. We have adopted the subgrid version of the SFINCS model. Based on the experiments presented by Van Ormondt et al. (2025) in the original subgrid paper for SFINCS, we have adopted a coarse-grid of 300m with a subgrid of 30m resolution. This is a tenfold subgrid-grid ratio of upscaling, which is shown to produce accurate results (Van Ormondt et al. 2025). This coarse grid amounts to 400,000 computational cells and about 800,000 cell-faces. The grid is developed in a projected coordinate system, in our case UTM39S.

In generation of subgrid, we have assigned the Manning's coefficient at the subgrid level based on the Copernicus LULC dataset at 100 m resolution (Buchhorn et al. 2020b). The land-use classes are interpolated to the 30 m subgrid using nearest neighbor interpolation. The table to convert the LULC classes to the corresponding Manning value is provided in the supplementary materials. Along the rivers, a Manning's n value of 0.035 is applied (Bunya et al. 2010).

While developing the subgrid tables, we have used the default 20 vertical levels. The subgrid table is generated using the HydroMT-SFINCS python toolbox (<https://github.com/deltares/hydromt-sfincs>).

4.3 Coupling between SCHISM-WWM and SFINCS

To drive the SFINCS compound flood model, we apply water level and wave setup extracted from the SCHISM-WWM along its open boundary (shown in Figure 3). Such coupling is known as one-way coupling (Xu et al. 2022) and a typical strategy with SFINCS (Eilander et al. 2023). Our open boundary is strategically chosen at 10-15 m water depth. At such depth, the wave setup contribution from SCHISM-WWM is found to be negligible (maximum 1-2 cm), thus allowing us to extract the tide-surge level. However, this also means that wave setup is not represented with only the extracted tide-surge water level. In our modeling framework, there could be two ways to do it - 1) extract the continuous wave setup at the coastline and add it to the tide-surge water level, 2) extract wave parameters from the SCHISM-WWM and apply an appropriate parametric method to estimate wave setup. Along the boundary of SFINCS, at each boundary point, the continuous sum of tide-surge level and wave setup then can be applied.

We choose the second approach here. We have found that due to the resolution, wave setup is vastly underestimated in SCHISM-WWM. Indeed, it has been shown that decametric resolution (or finer for steeper slopes) is required to properly simulate the wave-setup in coupled spectral model (Guérin et al. 2018), whereas our resolution in SCHISM-WWM is 500 m or coarser. Placing our boundary at a reasonably deep 10-15 m depth allowed us to extract the Significant Wave Height (H_s) and Mean Period (T_m) from SCHISM-WWM at the same location of the water level boundary and from these diagnose a more realistic wave setup using the parametric formulation of (Stockdon et al. 2006). This formulation has been used in global to local applications (Vitousek et al. 2017; Camus et al. 2021; Eilander et al. 2023), using Eqn. 8 –

$$\text{Wave setup} = 0.35\beta_f\sqrt{H_sL_0} \quad (8)$$

where, H_s and L_0 are deep-water wave height and wave length, respectively. L_0 is computed from the mean period using linear wave theory. A beach slope (β_f) of 0.045 is assumed here as suggested in Stockdon et al. (2006) for dissipative sites, which is typical of large portion of the world beaches (Aucan et al. 2018). Properly estimating the beach slope and wave setup requires dedicated field data collections and numerical modeling which is beyond our current reach. However, as such formulation is an approximation, we have tested various beach slopes (0.01 to 0.1), which does change the extreme water level (50 cm) but does not alter the

conclusions of our study, i.e., the flooding extent and the spatio-temporal role of compound factors in flooding, as discussed later.

4.4 Computation

SFINCS is written in Fortran, with OpenMP parallelization. We ran our model configuration in a 48-core Intel Skylake based node of a large cluster. Overall, the average time step of the model was between 6-8 sec, and 1-month of simulation took around 8 minutes in our computational configuration.

The model output from SFINCS subgrid model is stored in NetCDF files, at the coarse resolution grid (300 m). A high-resolution flood map (30 m) from the coarse model output is computed by superimposing the result on the subgrid bathymetry (30 m). Since, the model flow fields are adopted based on the subgrid bathymetry, this flood map estimate is more accurate than the LIE approach (Van Ormondt et al. 2025).

We have conducted several multi-year experiments (2019-2023) to assess the model's response to the rainfall dataset (ERA5, ERA5x2) and rainfall-runoff methods (CN-A, CN-B). For cyclone Batsirai, aside from the baseline experiments, we have also conducted experiments by turning on and off oceanic and continental factors to assess their individual contributions. A summary of these experiments is provided in Table 2.

Table 2. Summary of the numerical experiments. Long experiments are from 2019-2023. Batsirai experiments are from 01/01/2022 to 15/02/2022.

Experiment	Time period	Rainfall	Runoff method	Water level boundary
CN-A ERA5	Long	ERA5	CN-A	SCHISM-WWM
CN-B ERA5	Long	ERA5	CN-A	SCHISM-WWM
CN-B ERA5x2	Long	ERA5x2	CN-B	SCHISM-WWM
Baseline	Batsirai	ERA5x2	CN-B	SCHISM-WWM
Ocean only	Batsirai	None	N/A	SCHISM-WWM
Continent only	Batsirai	ERA5x2	CN-B	None

5 Results and Discussion

5.1 Long-term hydrograph

First, we assess the capacity of the SFINCS model to represent the rainfall-runoff processes over an extended period of time from January 2019 to December 2023. We focus on a location named KM47 (see Figure 3), along the course of Mananjary River, 47 km upstream of its mouth. This is the only location over our domain where the water level is monitored. The

observations are based on spaceborne altimetry distributed on Hydroweb (Crétaux and Calmant 2015). The time series of the water level at KM47 is shown in Figure 4. Two configurations of the infiltration method are tested here based on the CN method (Ponce and Hawkins 1996). The orange dashed line represents the hydrograph for our original curve number method without any recovery (CN-A ERA5), and the brown line shows the hydrograph for curve number method with recovery (CN-B ERA5). Blue line shows the model for CN-B but forced with bias-corrected ERA5 rainfall – CN-B ERA5x2 – according to the findings of Mazza and Chen (2023).

The very first observation from the hydrographs shown in Figure 4 is that the Mananjary River exhibits a very strong variability of water level at intra-monthly timescales. This is consistent with the physical geography of this mountainous region (Aldegheri 1972). The river baseflow water level is typically flat without much seasonality. On the other hand, episodic high-water events can gain as high as 20m additional water level - a feature well documented in this region (Aldegheri 1972).

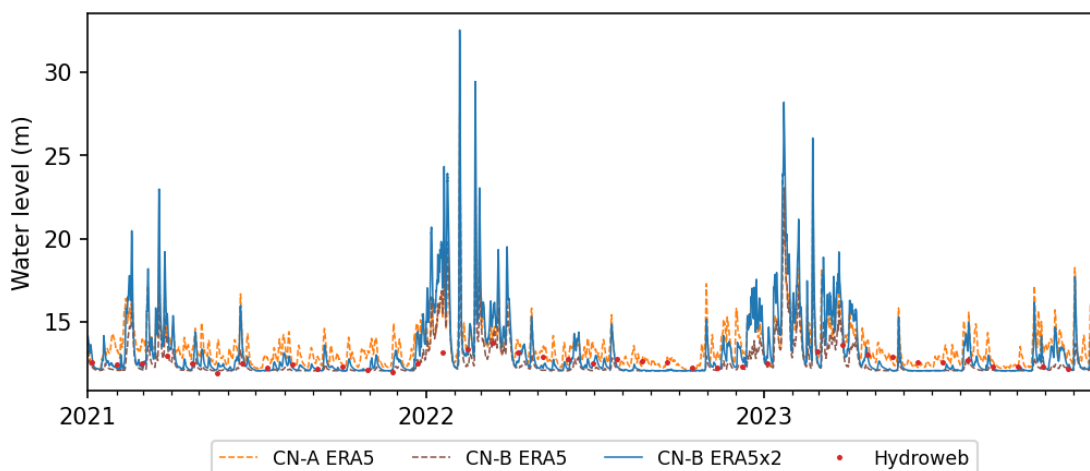


Figure 4. Timeseries of KM47 location at the upstream of the Mananjary River for simulation with ERA5 rainfall and curve number method without recovery (orange), curve number with recovery (brown), curve number with recovery and ERA5x2 rainfall (blue), altimetric virtual station from Hydroweb (red dots). A longer timeseries for 2019-2023 is shown in the supplementary materials (Figure S4).

The difference between the two run-off models is evident here not on the peak water levels but on the water level at baseflow. A larger baseflow water level for CN-A, and a flat base flow for the CN-B model are found. The intermittent spikes (following a dry spell) are much larger

in CN-A, suggesting the inability to capture the initial moisture retention of the system, which appears to be well represented in the CN-B model.

Between the two forcings of CN-B model - one with the raw ERA5 output (CN-B ERA5) and another with the bias corrected ERA5 (CN-B ERA5x2) - both show essentially the same baseflow water level response. For small rain events, the response is proportional to the change in the rainfall.

Validating water level in such an ungauged river basin is difficult. In the recent years, altimetry-derived water level has been found to be an efficient approach to obtain data in ungauged basins, where altimetric passes cross the rivers (Sun et al. 2012; Bogning et al. 2018; Andriambeloson et al. 2020; Kitambo et al. 2022). Such crossings are also known as virtual stations. One such virtual station monitored by Sentinel-3B satellite is currently being operationally distributed in Hydroweb (Santos da Silva et al. 2010; Crétau and Calmant 2015; Normandin et al. 2018) over Mananjary River at the KM47 location shown in Figure 3. The hydrograph from this dataset is shown in red dots. We applied a -0.94 m correction to reference the Hydroweb data from geoid to MSL - the datum of our model - through a linear interpolation of the CLS Mean Dynamic Topography dataset (Mulet et al. 2021). The water level estimate is available at this virtual station from 2019 to 2024 at a 1-month interval.

Strikingly, Hydroweb fails to observe the flooding events (e.g., January-February 2022). The maximum and minimum water level observed by Hydroweb is 13.45 m and 11.62 m respectively during the whole observation period. Such behavior is not consistent with the characteristics of basins prone to flash floods like that of Mananjary (Aldegheri 1972). This is linked to the processing chain of Hydroweb, which heavily relies on climatology and an aggressive outlier detection (J-F Crétau, personal communication, 2024). Hence, we only made a direct comparison with the results from the baseflow water level part of the model by filtering out the model outputs that fall outside the min-max values of the Hydroweb data (Not filtered in Figure 4). We computed the root mean squared error (RMSE) and bias relative to Hydroweb (Table 3). In our comparison, CN-A ERA5 shows an RMSE of 0.66 m with a bias of 0.52 m. The CN-B model with ERA5 improves the RMSE to 0.54 m and bias of 0.43 m. And finally, the bias-corrected ERA5x2 further improves the baseflow with a RMSE of 0.44 m and a bias of 0.36 m. In addition, sensitivity experiments with varying hydrographic depth ranging from 50% to 200% of the reference value shows that the model response remains robust (not shown). As the baseflow is well represented in the bias-corrected ERA5 (ERA5x2), we

only analyze the ERA5x2 experiments for subsequent analysis. The ability of the model to reproduce the altimetry derived water levels during baseflow increases our confidence in the vertical referencing of the bathymetric and topographic datasets, as well as the bias correction applied to the ERA5 dataset (e.g., ERA5x2).

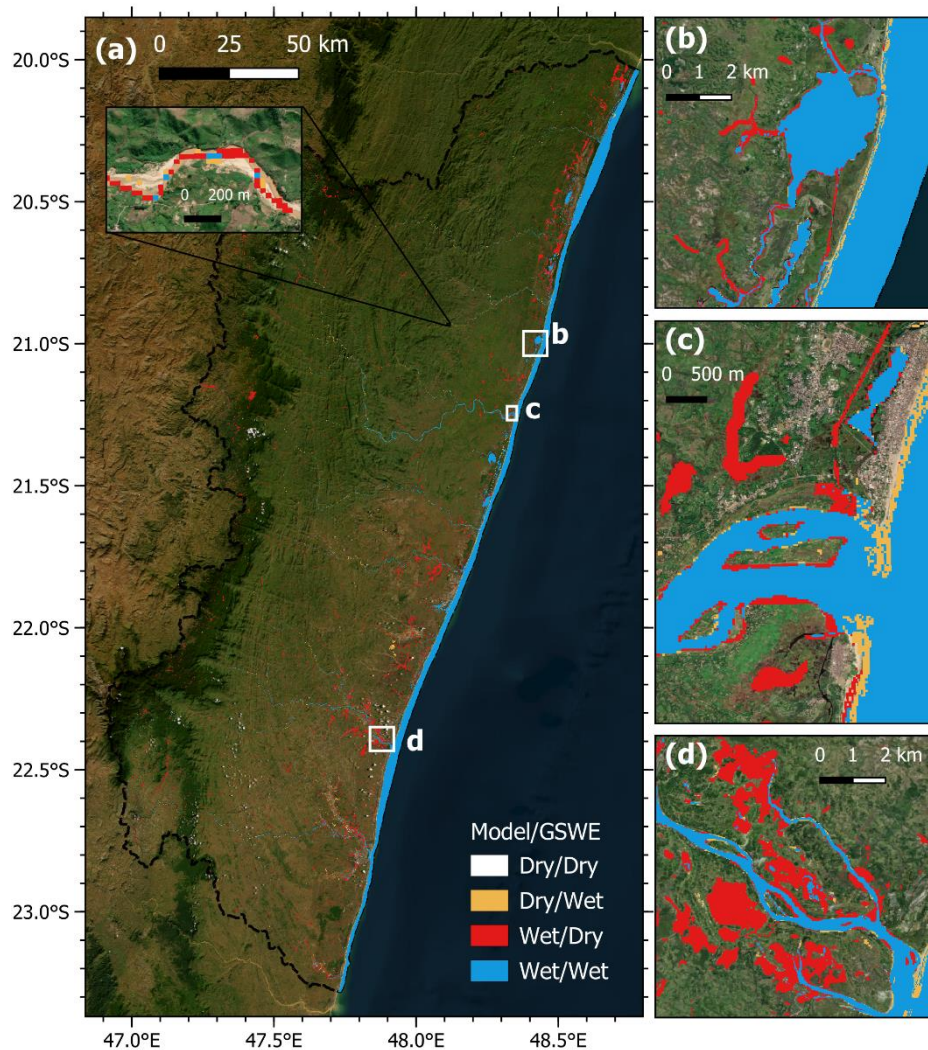
Table 3. Statistical comparison of the quality of baseflow in the long-term simulation for SFINCS.

Metric	CN-A ERA5	CN-B ERA5	CN-B ERA5x2
RMSE (m)	0.66	0.54	0.44
Bias (m)	0.52	0.43	0.36

5.2 Flood frequency evaluation

To further assess the characteristics of the model, we compared the water extent derived from our model to Global Surface Water Extent Dataset (GSWE) developed by Pekel et al. (2016) (Data retrieved from <https://global-surface-water.appspot.com/>). This dataset was originally developed based on the Landsat 5, 7, and 8 images from 1984 to 2015 with non-uniform global coverage. Recently this dataset was revised to cover the recent period till 2021. We have used the recurrence layer, which provides the yearly probability of a pixel being identified as water.

As cloud cover is an important limiting factor on the observability of the water extent (Pekel et al. 2016), for a reasonably accurate comparison, it requires that the model output is also subject to similar constraints. Over the modeled period (2019-2023), we first identified all the Landsat-8 images that cover our region of interest and filtered out the images which have 10% or more cloud cover. The model results from those timestamps are then used to compute the water extent. For this experiment, we have chosen 5 cm as threshold to identify an area to be flooded or not, which is within the typical range for compound flooding studies (Huang et al. 2021).



710

711 Figure 5. Comparison of water extent (>10% or more probability) in GSWE dataset with the
 712 extent derived from long-term simulation (CN-B ERA5x2).

713 From these two occurrence datasets - one from remote sensing and one from the model - we
 714 compared the water extent corresponding to 10% or more of flooding probability. Although
 715 both of the datasets are 30 m resolution, they are not in the same grid. For comparison GSWE
 716 dataset was re-projected in the model pixel grid with a bilinear interpolation. The comparison
 717 is shown in Figure 5 as binary analysis. A few areas of specific interest are shown in zoom
 718 (Figure 5b-d). The areas that are identified as dry in both model and GSWE are masked in the
 719 figure.

720 The areas which are identified as water in both datasets are shown in blue, which is the majority
 721 of the regions (nearshore ocean, rivers, channels). Orange pixels indicate the locations where
 722 the model suggests dry whereas the GSWE shows a wet pixel. This mismatch is consistent with
 723 the movement of the shoreline over the years that is not resolved in the GSWE dataset. This is

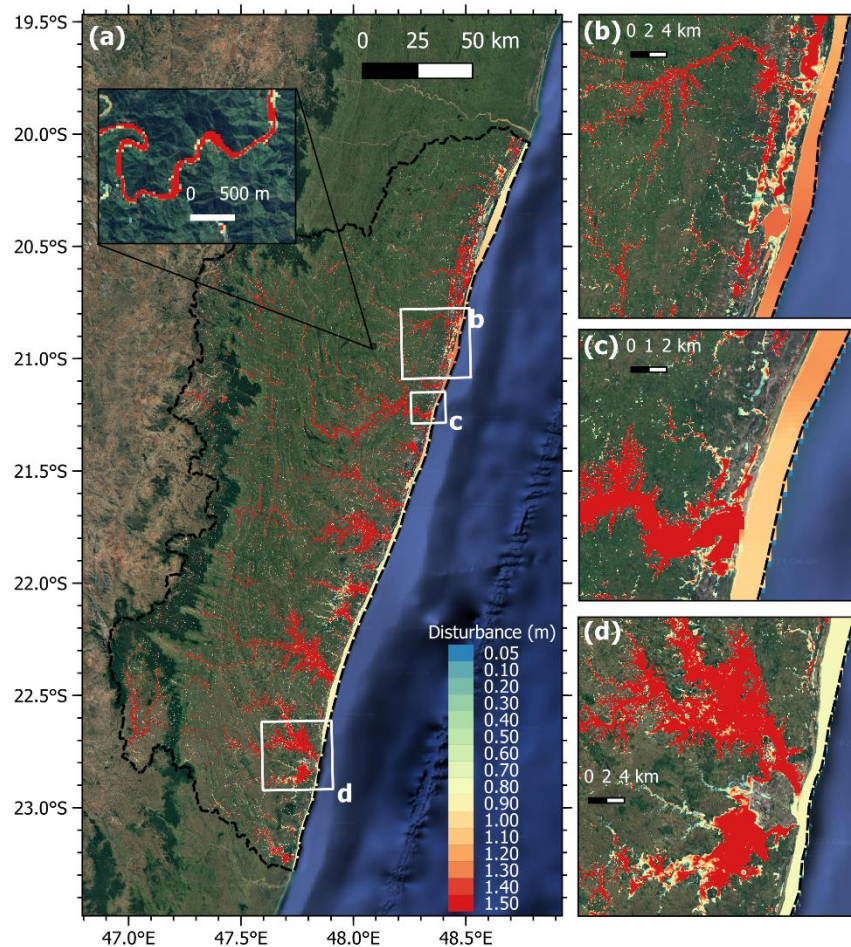
very clear in Figure 5c, where the sandbars closing the Mananjary River are correctly identified as dry (consistent with the satellite images of recent years; not shown), whereas GSWE identify them as flooded.

On the other hand, the red pixels indicate the areas that GSWE identified as dry, but the model identifies them as wet. Closer inspection of these regions from satellite imagery and a cross-referencing with the Copernicus LULC dataset (Buchhorn et al. 2020a, b) indicates many of those to be agricultural fields. Our topographic dataset is based on relatively recent acquisitions (i.e., TanDEM-X from 2015), with vegetation and building corrections applied based on recent land-cover dataset (also from 2015) (Hawker et al. 2022). Such that we can reasonably assume that the topography is more representative of the current period. Indeed, it is well documented that in Madagascar forests lands have been turned into agricultural land at an aggressive rate over the past decades (Vieilledent et al. 2018; Suzzi-Simmons 2023). As the GSWE data rely on observations from pre- and post-2000s, such land-use and land-cover change may contribute to some of the discrepancy between the model and the GSWE for the pixels that are identified as wet in the model but dry in GSWE.

Overall, the model seems to be able to capture the water extent quite well, including very narrow rivers (~50 m) as shown in the inset of Figure 5a.

5.3 Flooding during Batsirai

Analysis of long-term riverine water level and flood frequency maps discussed in the previous section confidence about the relevance of the choice of rainfall forcing as well as rainfall-runoff model. In this section, we focus on tropical cyclone Batsirai. We considered our CN-B ERA5x2 simulation. Along the coastal boundary, the tide-surge level and wave setup derived from the coupled SCHISM-WWM model are prescribed. For our experiments, SFINCS appears to be spun-up within 3 days of model simulation. In our application, the model is integrated from 2022-01-01 to 2022-02-15, well ensuring the dynamic adjustment of the model to the forcings.



749

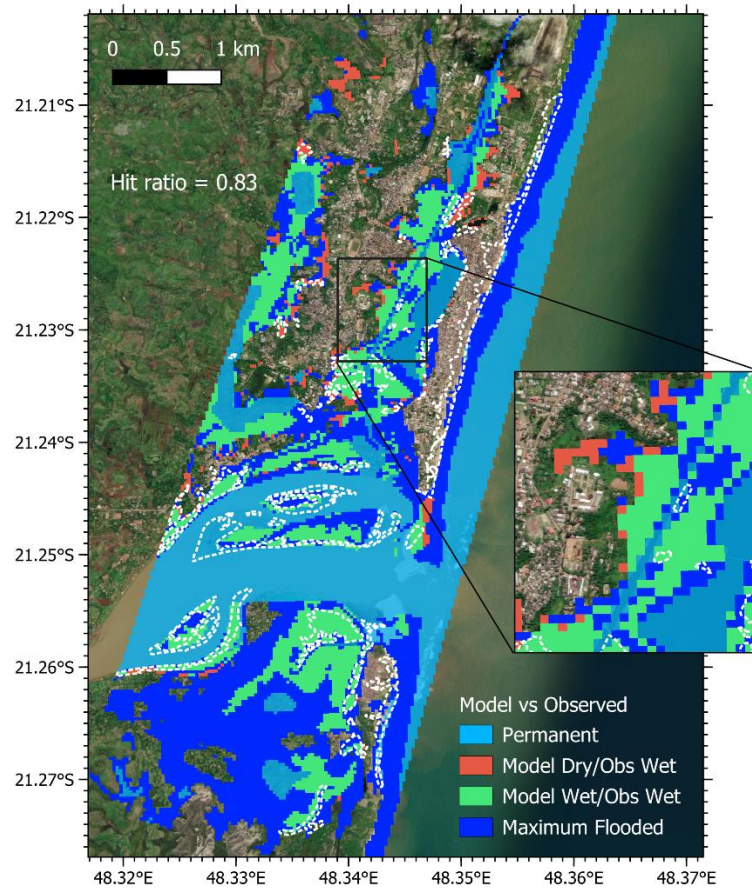
750 Figure 6. The maximum water extent modelled during Batsirai (2022-01-24 to 2022-02-11)
 751 over the whole model domain (a). The colorbar indicates the water level disturbance defined
 752 as the water level relative to mean sea level at the sea (topography ≤ 0) and water depth over
 753 the inland (topography > 0). Note that the colorbar is restricted to 1.5 m for clarity, but it can
 754 reach much higher (~10 m) over the inland. Two regions of maximum water levels in (b)
 755 Ambohitsara and (c) Mananjary, and a region with relatively minor surge in (d) Farafagna is
 756 shown in detail in the subpanels.

757 The flooding during cyclone Batsirai is expected to be spread over a domain that encompasses
 758 the land-ocean continuum. Over the continent, the relevant metric for flooding is the water
 759 depth (water level above the topography), whereas in the ocean the relevant metric is water
 760 level relative to MSL. Hence, to represent the flooding, we first define disturbance as the water
 761 depth over land wherever topography is positive, and water level above MSL over ocean (Krien
 762 et al. 2017b; Huang et al. 2021; Khan et al. 2022). The maximum disturbance is computed from
 763 the downscaling of modeled water level over subgrid topography during Batsirai (2022-01-24
 764 to 2022-02-11) and illustrated in Figure 6a. Previously used threshold water depth of 5 cm is
 765 also applied here to separate flooded and non-flooded areas. Additional panels show three
 766 different areas in detail - namely (b) Ambohitsara, (c) Mananjary, (d) Farafagana. Water depth

could be much higher in the rivers' reaches and inland due to the flashy nature of the rivers (order of 10 m). This is capped in the colorbar for clarity and illustrating the contrast of the water level along the coastline. The water level along the rivers will be further discussed later.

At first glance, our modeling shows a large-scale flooding, particularly along the reaches of the rivers. The flooding extent increases in the downstream regions due to accumulation of rainwater and flattening of the topography. Along the coast, the surge peak can be identified between Ambohitsara (Figure 6b) and Mananjary (Figure 6c) reaching about 1.35 m. Over Madagascar, lakes, low-lying lands and their surrounding areas are found to be severely flooded, which is clearly seen in Figure 6b near Ambohitsara. Cities that are built on relatively high-grounds (e.g., Farafagna in Figure 6d) appear to be surrounded by floodwater while the core of the cities remain above floodwater. Figure 6c shows Mananjary City, situated downstream of the Mananjary River by the coastline. The peak of the surge is not too far from the city (35 km). On the other hand, along the Mananjary River, we observe large-scale flooding similar to other rivers in this region. We further focus on this region and compare the observed and simulated water extent as shown in Figure 7.

The map of observed flooding extent over Mananjary is provided by Copernicus under an Emergency Management Service - Activation no. 564 (Copernicus 2022). The flood extent is derived from a post-event image collected on 2022-02-07 at 07:20 UTC (about 1.5 day after the cyclone landfall) observed by WorldView-2 satellite. The pre-event image is taken on 2021-08-07 at 06:56 UTC by WorldView-1 satellite. Both of these satellites collect images at 50 cm spatial resolution. We compared the flooded areas extracted by Copernicus with the flooding extent in the model at the same date as the post-event image. As the imagery does not provide any water depth, the comparison is done only based on the water extent as binary (flooded vs non-flooded). In Figure 7, the light-blue indicates the permanent water bodies (e.g., rivers, lake, and ocean). The pixels where both the model and observation agree are shown in green, and where they disagree are shown in red. In addition, the imprint of the maximum flooded area in the model (Figure 6) is also shown in dark blue (hence red and dark blue combined is the maximum flooding extent).



795

796 Figure 7. Comparison with the satellite observation from the Copernicus Emergency Service
 797 (Copernicus 2022) over Mananjary City derived from WorldView satellite (Pre-event image:
 798 2021-08-07, Post-event image: 2022-02-07). For comparison, the results from the model at the
 799 same time are used. Light green shows the areas that are correctly identified (model wet,
 800 observation wet), and flooding in the red areas is not captured by model (false dry). White
 801 outlines show the areas that are identified with traces of flood from visual interpretation (but
 802 not flooded in the post-event image). Blue shows the maximum outline of flooding from the
 803 model considering the whole period of TC Batsirai (28/01/2022 to 11/02/2022).

804 For a statistical assessment, we have computed the hit ratio for the flooded areas (without
 805 permanent water bodies). Hit ratio here is defined as the number of pixels in green (flooded
 806 areas identified by the model) divided by sum of red and green (flooded areas identified by the
 807 observation). The value ranges from 0 to 1 with 0 indicating no match between observed and
 808 the model and 1 indicating a perfect match.

809 Overall, the model shows a very good agreement with the observed flooding extent over the
 810 domain with a hit ratio of 0.83. It means the model under-predicts some of the flooding. A
 811 closer look at the dry errors (red pixels) shows that many of these are located at the edge of the
 812 observed flooding extent with 1-pixel width (30 m). Such single-pixel error is typical when

comparing relatively coarse fields (model, 30 m) with a much finer one (WorldView, 50 cm). On the other hand, a large extent of flooded area is not captured by the image as shown by the blue shaded areas, possibly linked to the acquisition of post-event image much later than the cyclone landfall. Particularly there is a wide zone of flooding just to the south of Mananjary City (around 21.24°E, 48.34°E) as well as over the agricultural land on the southern bank of the river (21.27°S-21.26°S, 48.32°E-48.34°E).

In addition, the flood extent, the visually delineated boundaries of impacted areas (flood traces) are also provided with the mapping by Copernicus (Copernicus 2022). These blocks are shown in white dashed outlines in Figure 7. Most of these areas are captured by our model except along the coastline. Such reported flood traces are potentially due to wave-runup, a process that does not exist in our current modeling framework – hence a limitation of the current modeling which is discussed later. These modeled flood maps were found to be robust in a sensitivity testing with another model configuration with twice as fine grid size (viz. 150 m, not shown).

A cross-comparison with the LULC dataset of Copernicus (Buchhorn et al. 2020b) and the flooded area reveals that about 30% and 27% of the flooded areas are classified there as vegetation and agricultural fields respectively. The largest portion, about 42%, is classified as forests. The rest, less than 1%, is classified as built-up areas. Indeed, in disaster reports, large scale damages to crops and agricultural fields were reported (OCHA 2022a; WMO 2022). However, these estimates should be considered with caution. Our LULC dataset is based on 2015, which does not capture any recent conversion of forests to agricultural fields. Pixels that are identified as vegetation, also often get misclassified instead of agricultural lands. Overall, we can conclude that the flooding induced by TC Batsirai significantly affected the agricultural lands through large-scale flooding.

5.4 Role of compounding factors

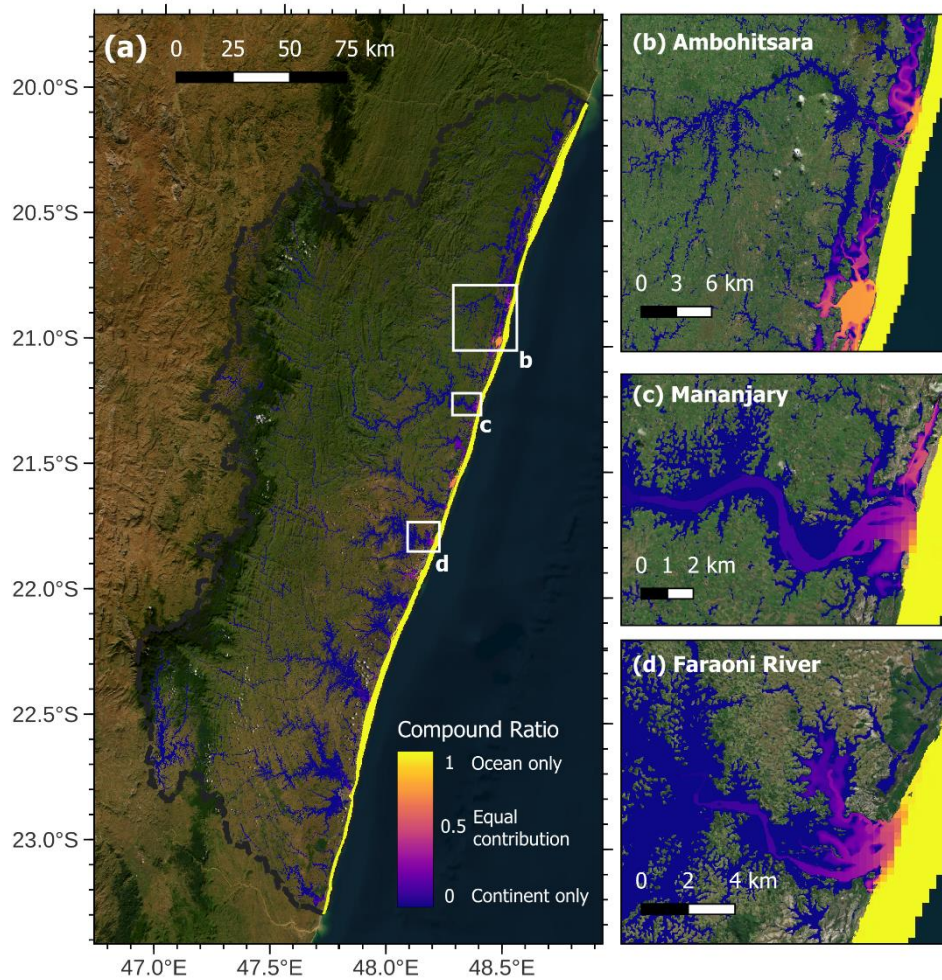
In this section, we assess the individual contribution from the oceanic and continental factors to ascertain the mechanism of compound flooding. From the oceanic side, we have accounted for tide, storm surges, and wave-setup. They will be treated as one single term – oceanic factor. On the other hand, the processes considered over the continent are encapsulated in another single term, which we call continental factor. In our model configuration, the Mananjary watershed is a self-contained system from the point of view of hydrology. By forcing the model with rainfall and accounting for losses, the model could simulate the necessary rainfall-runoff processes. In other words, by designing our watershed as self-contained, we got rid of the need

for external river discharge input (Huang et al. 2023), in contrast to other studies (Zhang et al. 2020b; Huang et al. 2021; Eilander et al. 2023).

As we are modeling a dynamic system – the oceanic and continental factors will interact with one another. Such interaction could be non-linear in nature, so that the sum of the individual terms does not add up to the total water level (Huang et al. 2021; Khan et al. 2021). To make the analysis more legible, we split our analysis into two parts. First, we analyze the contribution of the two factors without considering any interaction between them. This will evidence the individual role of each of the factors. Then, for the second analysis, we compare the total water level to the individual sum of the water levels from oceanic and continental factors. This will allow us to assess the potential non-linearities of their interaction.

For the first analysis, we conducted two simulations. In the first simulation without continental factors – termed as "Ocean only" in Table 2 – we have turned off the rainfall input, keeping only the oceanic water level boundary (tide, storm surges, wave-setup). The second simulation without oceanic factors – termed as "Continent only" – contains only rainfall as forcing with the oceanic water level boundary set to zero. A linear sum of the water level computed in these two simulations gives us a total water level that does not contain any non-linear interaction (TWL_{linear}). Figure 8 shows the ratio between the maximum of (TWL_{linear}) and the maximum of water level computed in the Only Ocean simulation. A value of 1 in Figure 8 means the maximum water level is coming fully from the ocean (yellow). On the other hand, 0 means the maximum water level is fully due to the continental processes.

In general, the maximum water level in the large part of the ocean and inland is caused by their respective factors, as one would expect. Along the shoreline, a relatively narrow region is observed where both factors interact and significantly contribute. A few of those regions are shown in detail in Figure 8, over (b) Ambohitsara, (c) Mananjary, (d) Faraoni. These locations are selected around the location of maximum water level in Figure 6, where the oceanic water level is larger, hence the contribution is more legible.



871

872 Figure 8. Compound ratio computed as the ratio of maximum disturbance computed for “Ocean
 873 only” simulation to the maximum disturbance from the linear sum of “Ocean only” and
 874 “Continent only” simulation over model domain (a) Zoomed areas indicate some of the notable
 875 areas - (b) Ambohitsara and the zone of maximum storm surge, (c) Mananjary City along the
 876 Mananjary River, and (d) Faraoni River where storm surge was minor but with large
 877 hydrological signature.

878 For the larger rivers, e.g., in Figure 8c,d, there is a gradual change in the role of contribution
 879 (oceanic to continental) from the outlet to the upstream of the estuaries mouth. Up until about
 880 5-8 km inside the estuaries the ocean clearly contributed to the maximum water level. Clearly,
 881 this interaction is more important in the regions affected by storm surge and wave setup. For
 882 example, in Figure 8b, which is located in the vicinity of the storm surge maximum, a strong
 883 oceanic contribution in the lagoons and small coastal channels could be seen. Overall, both
 884 oceanic and continental factors are found to be significantly contributing to the flooding hazard
 885 during cyclone Batsirai. Although the oceanic factors become more important along the
 886 coastline, particularly around the location of landfall, the major continental flooding is caused

by cyclone-induced rainfall-runoff. In other words, the overall flooding hazard in our study domain is clearly compound in nature.

5.5 Non-linearity of compound factors

In the previous section, we analyzed the total water level without considering the non-linear interaction between the factors (TWL_{linear}). However, the dynamics of the total oceanic water level during storm events along the coastline is known to be non-linear. One such example is the tide-surge interaction (Idier et al. 2012; Krien et al. 2017b), where the change in background sea level triggers a change in tide (Khan et al. 2020), which subsequently changes the total water level (Khan et al. 2021). In this study, we focus on the non-linearity of contribution between only the two compounding factors, i.e., the oceanic factor considered as a whole, and the continental factor.

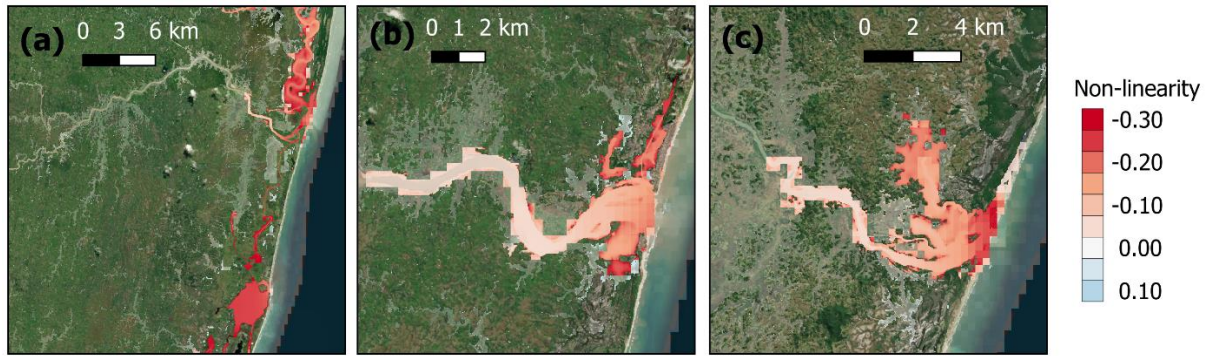


Figure 9. Spatial distribution of non-linearity for the zoomed region shown in Figure 8. Any region other than yellow indicates areas with non-negligible non-linear compound effect.

Here we assess the non-linear interaction between the compounding factors by taking the ratio between the maximum water level from the full SFINCS (TWL_{full}) model and the individual sums (TWL_{linear}) and its deviation to unity. The non-linearity metric reads as in Eqn. 9 –

$$Non - linearity = \frac{TWL_{full}}{TWL_{linear}} - 1 \quad (9)$$

The computed non-linearity is illustrated in Figure 9 for the three regions highlighted in Figure 8b-d. A value close to unity indicates that there is no significant non-linearity among the two compound factors. A positive non-linearity means TWL_{full} is larger than TWL_{linear} , and the opposite for a negative non-linearity. Where the compound ratio in Figure 8 is 0 (Ocean only) or 1 (Continent only), the non-linearity is 0 – i.e., independent factors, hence no non-linearity. This is the case for most of our model domain. Expectedly, non-linearity between factors is

only meaningful when there is significant contribution from both of the factors as seen in Figure 9. We see that they have different patterns based on the area of focus. In Ambohitsara (Figure 9b), strong negative non-linearity is observed in the backwater along the coastline where the TWL_{full} is significantly smaller than the TWL_{linear} , as much as 30%. Over Mananjary (Figure 9b), the negative non-linearity decreases from the mouth of the Mananjary River (-0.15) to about 8 km upstream (-0.05 to 0). A very high negative non-linearity is seen in the lakes and floodplains (-0.25 to -0.30) similar to Ambohitsara. The scenario is not so different in the Faraoni River (Figure 9c) albeit with a stronger negative non-linearity at the coast (-0.20 to -0.25) which vanishes about 10 km upstream of the river.

In general, in the coastal region the non-linearity ratio is negative (supplementary Figure S4). This means that for TC Batsirai the non-linear interactions between the oceanic and the continental factors consistently act to reduce the total water level.

5.6 Compound timing of the flooding

One important facet of compound flooding is the occurrence of consecutive flooding caused by flood peaks that take place at different times under the influence different drivers. Here, we examine whether the flooding that occurred during cyclone Batsirai shows such behavior. For this analysis, we kept our focus on the Mananjary River where we have previously compared our modeling with observations (both low-flow hydrology and flood extent). To analyze the water level characteristics, we have extracted a set of modeled water level timeseries during cyclone Batsirai along the river channel as shown in Figure 10a. The locations are marked with a prefix - KM - followed by the distance from the shoreline. For example, KM3 means the location is 3 km inland from the shoreline, whereas KM-0.5 means the location is 500 m offshore from the shoreline. The shoreline point, which is located between KM0.4 and KM-0.5, is shown in the inset panel in Figure 10a. For clarity, the water level evolution from KM47 (the most upstream) to KM2 are shown in a separate panel (Figure 10c) from KM0.4 to KM-0.5 (Figure 10b). Cyclone Batsirai made landfall around 16:00 UTC on 5th of February 2022, which is indicated in red dashed vertical line.

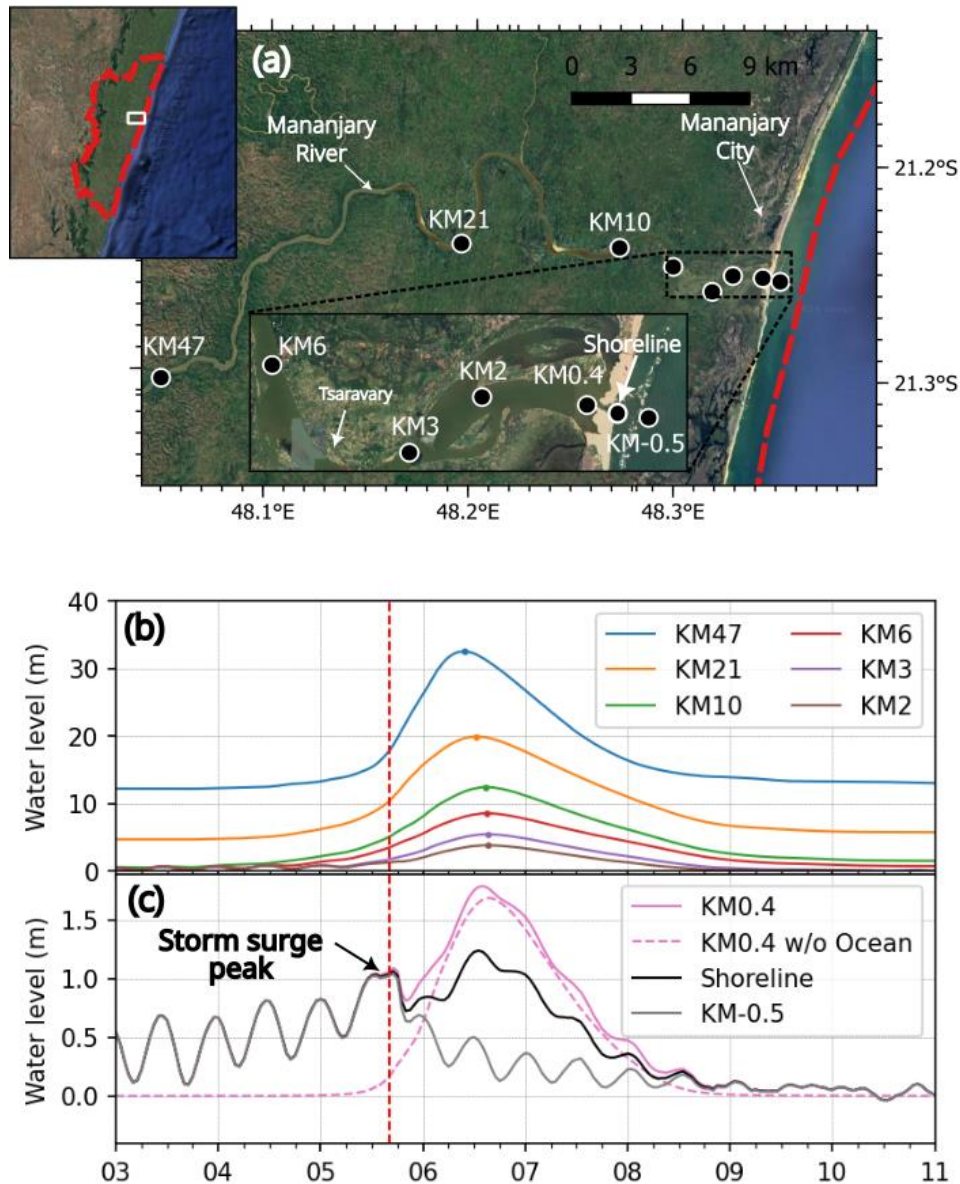


Figure 10. (a) The location of the virtual stations along Mananjary River. The stations are named based on their distance from the Shoreline in kilometer (e.g., KM47 is 47 km inland, KM-0.5 is 0.5 km offshore). The timeseries of flood hydrograph from (b) KM47 to KM2, which is shown separately in from (c) the three stations around the Shoreline. In addition, the water level from Continent only experiment is shown for KM0.4 with pink dashed line (KM0.4 w/o Ocean) in panel c. The red vertical in b-c indicates the time of the landfall of cyclone Batsirai.

At KM47, the most upstream location, we observe a water level rise of about 20 m during the event. As discussed before, such a sudden and sharp rise is typical of this region and similar sudden rises have been reported in the region in the past during extreme events (Aldegheri 1972). This bulge of water can be considered solely generated by the heavy rainfall that accompanied cyclone Batsirai. As it propagates towards the outlet, the peak progressively flattens and its magnitude is roughly reduced to half at KM21. Between KM6 and KM3, the riverine flood water level starts to be affected by the oceanic tide, as seen from the consistent

semi-diurnal oscillations. At Tsaravary, a small-town east of Mananjary and nearby station KM3, a water level rise of 3 m is reported, which corresponds well to the modeled water level (OCHA 2022a).

The tidal influence is more clearly visible in the bottom panel at KM0.4, Shoreline, and KM-0.5. At KM0.4, before the inland flood water reaches, the water level follows essentially the same tidal water level as offshore (KM-0.5). At the time of landfall, we see a peak of about 1.1 m, that comes from the oceanic surge. This peak is then followed by a much larger peak of about 1.9 m that corresponds to the upstream floodwater rushing through the river. The shape of this peak is significantly distorted by its non-linear interaction with the ocean. This becomes clear when compared to the water level at KM0.4 for Continent only experiment (KM0.4 w/o Ocean). This distortion becomes more prominent for the water level at Shoreline (black).

The floodwater takes about 6 hours to travel from the upstream location (KM47) to the coastline. Consequently, at the coastline around Mananjary City, the maximum storm surge (along the coastline) occurs more than 18 hours before the water level in the rivers rises to its maximum, consistent with the field reports (WMO 2022). This characteristic of the compound flooding and its impact conforms with local testimonies of Mananjary during the disaster (Reuters 2022).

5.7 Limitations

Like any other modeling work, our study is not void of limitations. An important limitation over our study domain is the lack of observational, consistent substantiation of the water level variability. We have tried our best to compare our model results with as many observations as possible, including remote sensing water level, water extent, flood extent, and reported water height. However, it would be ideal to have more synoptic data for comparison. In this regard, more detailed analysis would be possible with the new generation of altimeters such as Interferometric-SAR in Surface Water Ocean Topography (SWOT) has a great potential.

The current configuration of the coupled circulation model (SCHISM-WWM) potentially does not have enough resolution to resolve the wave breaking processes and associated wave-setup, although this is considered to some extent by adding parametric wave setup in the one-way coupling through a boundary condition. However, this approach has known limitations (Aucan et al. 2018), mostly related to the use of a constant beach slope, which is a key parameter for wave setup development (Martins et al. 2022).

While comparing with the remote sensing derived flood map, we observed that along the coastline there are reported flood traces, where in the model only minor flooding occurs. This is potentially due to wave run-up, a process not represented in phase-averaged models like SCHISM as discussed in Bertin et al. (2014). Again, relying on the parametric formula of Stockdon et al. (2006), one could estimate a run-up in the order of 4 m, which is the typical elevation of the zone with flood trace.

Overall, we have used various assumptions for the input bathymetric and topographic data, atmospheric forcing, and hydrologic properties. Each of these assumptions can be criticized as limitations. They may be addressed as new datasets become available over the area in the future.

6 Conclusions

In this study, we assessed the dynamics of compound flooding during cyclone Batsirai in the Mananjary Basin in Madagascar. The scarcity of reliable data posed significant challenges, necessitating several practical assumptions in our modeling approach. Despite those constraints, our findings underscore the critical importance of incorporating compound flooding processes to accurately evaluate TC-induced flooding hazards over Madagascar.

Our results highlight the joint roles of oceanic and continental factors in driving TC-induced flooding, with oceanic contribution typically extending up to 10 km upstream along the rivers. TC-induced rainfall and runoff jointly emerge as the dominant drivers of inland flooding, while along the coast, both oceanic and continental factors contribute. Notably, our analysis revealed that the timing of flooding from oceanic and continental factors is asynchronous along the rivers. For example, in the Mananjary River, the floodwaters from the watershed reach Mananjary City, located at the river mouth, about 18 hours after the peak oceanic surge event. At the coastline, the magnitudes of both surge peak and riverine flood water peak are comparable (1-1.3 m). This consecutive flooding pattern aligns with reports from the affected communities (Reuters 2022), emphasizing the necessity of considering compound flooding in hazard assessments to capture the nature of the physical hazards that is compatible with people's perception and relevant human exposure.

We showed that along the coastline the compound flood water level has a non-linear behavior, indicating interaction between oceanic and continental factors. For cyclone Batsirai, the non-linear interaction is found to be affecting negatively the total water level, with negative non-

linearity reaching as much as -0.30. In other words, the total water level is 30% less than the summation of the individual factors. However, the non-linearity is expected to be different for different events, which may depend on the phase and amplitude of the tidal water level at the time of landfall (Krien et al. 2017b), as well as with the interaction of riverine flood water. Given the diversity of tides from micro-tidal to macro-tidal around Madagascar, such non-linear factors may become even more important in the other watersheds of the island.

Our modeling platform showed reasonable capability in simulating the observed flooding patterns at fine spatial resolution (30 m). In this study, we have focused on one particular basin – Mananjary – where cyclone Batsirai made landfall. The same methodology that has been developed and demonstrated here can be applied over the other basins of Madagascar for a nation-scale assessment of TC-induced flooding. Furthermore, being largely based on global remote-sensing derived datasets, the overall modeling framework presented here could easily be implemented for any cyclone impacted regions in the world. In data poor regions, the limited availability of ocean bathymetry data of acceptable quality may potentially be one of the remaining challenges (Krien et al. 2016), in addition to in situ observed water levels for calibration/validation of the modeling framework.

The perspective development of a Madagascar-scale modeling framework is challenging yet needed as the whole island is exposed to intense TC activities (Figure 1). In fact, cyclone Batsirai was accompanied by two other cyclones. Cyclone Ana (2022) made landfall only a week before the genesis of cyclone Batsirai and caused significant flooding and landslides in the northern parts of Madagascar. Notably, the capital of Madagascar Antananarivo was significantly impacted affecting more than 58 thousand people (OCHA 2022c; Li et al. 2023). On the other hand, cyclone Emnati made landfall in the southern parts of Madagascar on February 24, 2022 – only 18 days after cyclone Batsirai, claiming 15 lives and significant damages (OCHA 2022d). At least 60 thousand hectares of rice fields are reported to be flooded twice during these events. Overall these events have reported to impact half a million people (OCHA 2022c, d). The socio-economic impacts of such consecutive events are currently not well understood, and a national-scale compound flood model can significantly help to ascertain the impact of TC-induced flooding. In view of this, the fine scale hazard assessment made in the present study paves the way for evaluating flood risks and exposures at household scales across Madagascar (Hawker et al. 2024). A dedicated household scale survey is currently undergoing over Mananjary with an explicit objective to better understanding the prevalent climate migration driven by floods. The modeling framework developed in this work is

expected to provide an appropriately resolved hazard layer that is compatible with this overarching multi-disciplinary research goal.

One important open question in TC-hazards community is the role of climate change. In response to global warming, the current knowledge is that the TCs will become more intense, and more precipitation-laden (Knutson et al. 2020; Emanuel 2021; Bloemendaal et al. 2022). The impact of such trend is already making compound flooding more pronounced (Wahl et al. 2015). In addition, sea level rise due to climate change will not only directly contribute to overall flooding (Vitousek et al. 2017), but also can significantly change the underlying drivers such as tide (Pickering et al. 2017; Khan et al. 2020). Understanding such climatic hazards often requires simulating very long time periods for probabilistic assessment (Mentaschi et al. 2023), or thousands of individual storms for more robust probabilistic-deterministic assessment (Krien et al. 2017a; Khan et al. 2022). Being computationally efficient, the modeling strategy developed in the current study can facilitate such assessments in the future, which is essential for an informed future flood risk management and climate resilient planning in Madagascar and similar cyclone-prone regions.

Overall, our study paves the path forward to not only assessing the TC-induced compound flooding hazards but also understanding the socio-economic impacts from extreme events over Madagascar at a fine spatial and temporal scale. We expect this study to simulate more interest towards compound flooding and its impacts in least-studied regions like Madagascar.

Acknowledgements The authors extend their gratitude to Nicolas Pouvreau (Shom) for providing the tide gauge data at Toamasina, as well as to both Nicolas Pouvreau and Gaël André (Shom) for their valuable guidance on converting CD to MSL. We acknowledge the help of Florent Lyard (LEGOS) for his help with chart dataset. We also thank Stéphane Calmant and Jean-François Crétaux (LEGOS) for their insightful input on the Hydroweb dataset. We acknowledge Laurent Testut (LIENSs) for his contributions to the development of the original pyAltide methodology. Finally, we thank Marie-Dominique Leroux (Météo-France) for sharing their work on rainfall climatology over the Southern Indian Ocean.

References

- AghaKouchak A, Chiang F, Huning LS, et al (2020) Climate extremes and compound hazards in a warming world. *Annu Rev Earth Planet Sci* 48:519–548. <https://doi.org/10.1146/annurev-earth-071719-055228>
- Ahuja L, Cassel D, Bruce R, Barnes B (1989) Evaluation of spatial distribution of hydraulic conductivity using effective porosity data. *Soil Sci* 148:404–411
- Alam E, Dominey-Howes D (2014) A new catalogue of tropical cyclones of the northern Bay of Bengal and the distribution and effects of selected landfalling events in Bangladesh. *Int J Climatol* 35:801–835. <https://doi.org/10.1002/joc.4035>
- Aldegheri M (1972) Rivers and streams on Madagascar. In: *Biogeography and ecology in Madagascar*. Dr. W. Junk, La Haye, pp 261–310
- Andreadis KM, Schumann GJ-P, Pavelsky T (2013) A simple global river bankfull width and depth database: data and analysis note. *Water Resour Res* 49:7164–7168. <https://doi.org/10.1002/wrcr.20440>
- Andriambeloson JA, Paris A, Calmant S, Rakotondraompiana S (2020) Re-initiating depth-discharge monitoring in small-sized ungauged watersheds by combining remote sensing and hydrological modelling: a case study in Madagascar. *Hydrol Sci J* 65:2709–2728. <https://doi.org/10.1080/02626667.2020.1833013>
- AON (2022) Global catastrophe recap: first half of 2022. AON
- Aucan J, Hoeke RK, Storlazzi CD, et al (2018) Waves do not contribute to global sea-level rise. *Nat Clim Change* 9:2–2. <https://doi.org/10.1038/s41558-018-0377-5>
- Bates PD, Horritt MS, Fewtrell TJ (2010) A simple inertial formulation of the shallow water equations for efficient two-dimensional flood inundation modelling. *J Hydrol* 387:33–45. <https://doi.org/10.1016/j.jhydrol.2010.03.027>

- 1099 Battjes JA, Janssen JPFM (1978) Energy loss and set-up due to breaking of random waves. In:
1100 Coastal Engineering 1978. American Society of Civil Engineers, Hamburg, Germany, pp
1101 569–587
- 1102 Bernard A, Long N, Becker M, et al (2022) Bangladesh’s vulnerability to cyclonic coastal
1103 flooding. *Nat Hazards Earth Syst Sci* 22:729–751. [https://doi.org/10.5194/nhess-22-729-](https://doi.org/10.5194/nhess-22-729-2022)
1104 2022
- 1105 Bertin X, Li K, Roland A, et al (2014) A modeling-based analysis of the flooding associated
1106 with Xynthia, central Bay of Biscay. *Coast Eng* 94:80–89.
1107 <https://doi.org/10.1016/j.coastaleng.2014.08.013>
- 1108 Beucher F (2010) *Météorologie tropicale : des alizés au cyclone*. Météo-France, France
- 1109 Bevacqua E, Maraun D, Vousdoukas MI, et al (2019) Higher probability of compound flooding
1110 from precipitation and storm surge in Europe under anthropogenic climate change. *Sci*
1111 *Adv* 5:. <https://doi.org/10.1126/sciadv.aaw5531>
- 1112 Bevacqua E, Vousdoukas MI, Zappa G, et al (2020) More meteorological events that drive
1113 compound coastal flooding are projected under climate change. *Commun Earth Environ*
1114 1:47. <https://doi.org/10.1038/s43247-020-00044-z>
- 1115 Bidlot J (2012) Present status of wave forecasting at ECMWF. In: *Workshop on ocean waves*.
1116 pp 25–27
- 1117 Bidlot J, Janssen P, Abdalla S, Hersbach H (2007) A revised formulation of ocean wave
1118 dissipation and its model impact. ECMWF Reading, UK
- 1119 Bié AJ, de Camargo R (2023) Tropical cyclones position and intensity in the Southwest Indian
1120 Ocean as represented by CFS and ERA5 atmospheric reanalysis datasets. *Int J Climatol*
1121 43:4532–4551. <https://doi.org/10.1002/joc.8101>

- 1122 Bié AJ, de Camargo R, Mavume AF, Harari J (2017) Numerical modeling of storm surges in
1123 the coast of Mozambique: the cases of tropical cyclones Bonita (1996) and Lisette (1997).
1124 *Ocean Dyn* 67:1443–1459. <https://doi.org/10.1007/s10236-017-1095-7>
- 1125 Bloemendaal N, Moel H de, Martinez AB, et al (2022) A globally consistent local-scale
1126 assessment of future tropical cyclone risk. *Sci Adv* 8:.
1127 <https://doi.org/10.1126/sciadv.abm8438>
- 1128 Bogning S, Frappart F, Blarel F, et al (2018) Monitoring water levels and discharges using
1129 radar altimetry in an ungauged river basin: the case of the Ogooué. *Remote Sens* 10:350.
1130 <https://doi.org/10.3390/rs10020350>
- 1131 Bouwer LM, Jonkman SN (2018) Global mortality from storm surges is decreasing. *Environ*
1132 *Res Lett* 13:014008. <https://doi.org/10.1088/1748-9326/aa98a3>
- 1133 Brooke SAS, Ganti V, Chadwick AJ, Lamb MP (2020) Flood variability determines the
1134 location of lobe-scale avulsions on deltas: Madagascar. *Geophys Res Lett* 47:.
1135 <https://doi.org/10.1029/2020gl088797>
- 1136 Buchhorn M, Lesiv M, Tsendbazar N-E, et al (2020a) Copernicus global land cover layers—
1137 Collection 2. *Remote Sens* 12:1044. <https://doi.org/10.3390/rs12061044>
- 1138 Buchhorn M, Smets B, Bertels L, et al (2020b) Copernicus global land service: land cover
1139 100m: collection 3: epoch 2015: Globe
- 1140 Bunya S, Dietrich JC, Westerink JJ, et al (2010) A high-resolution coupled riverine flow, tide,
1141 wind, wind wave, and storm surge model for Southern Louisiana and Mississippi. Part I:
1142 model development and validation. *Mon Weather Rev* 138:345–377.
1143 <https://doi.org/10.1175/2009MWR2906.1>
- 1144 Camus P, Haigh ID, Nasr AA, et al (2021) Regional analysis of multivariate compound coastal
1145 flooding potential around Europe and environs: sensitivity analysis and spatial patterns.
1146 *Nat Hazards Earth Syst Sci* 21:2021–2040. <https://doi.org/10.5194/nhess-21-2021-2021>

- 1147 Copernicus (2022) EMSR564: Tropical cyclone Batsirai in Madagascar
- 1148 Couasnon A, Eilander D, Muis S, et al (2020) Measuring compound flood potential from river
1149 discharge and storm surge extremes at the global scale. *Nat Hazards Earth Syst Sci*
1150 20:489–504. <https://doi.org/10.5194/nhess-20-489-2020>
- 1151 Crétaux J-F, Calmant S (2015) Hauteur des lacs et des fleuves
- 1152 Daniel P, Haie B, Aubail X (2009) Operational forecasting of tropical cyclones storm surges
1153 at Meteo-France. *Mar Geod* 32:233–242. <https://doi.org/10.1080/01490410902869649>
- 1154 Dasgupta S, Laplante B, Murray S, Wheeler D (2010) Exposure of developing countries to sea-
1155 level rise and storm surges. *Clim Change* 106:567–579. [https://doi.org/10.1007/s10584-](https://doi.org/10.1007/s10584-010-9959-6)
1156 010-9959-6
- 1157 Eilander D, Couasnon A, Leijnse T, et al (2023) A globally applicable framework for
1158 compound flood hazard modeling. *Nat Hazards Earth Syst Sci* 23:823–846.
1159 <https://doi.org/10.5194/nhess-23-823-2023>
- 1160 Eldeberky Y (1996) Nonlinear transformation of wave spectra in the nearshore zone. PhD
1161 Thesis, IHE Delft
- 1162 Emanuel K (2021) Response of global tropical cyclone activity to increasing CO₂: results from
1163 downscaling CMIP6 models. *J Clim* 34:57–70. <https://doi.org/10.1175/jcli-d-20-0367.1>
- 1164 Emanuel K, Rotunno R (2011) Self-stratification of tropical cyclone outflow. Part I:
1165 implications for storm structure. *J Atmospheric Sci* 68:2236–2249.
1166 <https://doi.org/10.1175/jas-d-10-05024.1>
- 1167 Fassoni-Andrade AC, Durand F, Azevedo A, et al (2023) Seasonal to interannual variability of
1168 the tide in the Amazon Estuary. *Cont Shelf Res* 255:104945.
1169 <https://doi.org/10.1016/j.csr.2023.104945>

- 1170 Fitchett JM, Grab SW (2014) A 66-year tropical cyclone record for South-East Africa:
1171 temporal trends in a global context. *Int J Climatol* 34:3604–3615.
1172 <https://doi.org/10.1002/joc.3932>
- 1173 Fox-Kemper B, Hewitt HT, Xiao C, et al (2021) Ocean, Cryosphere and Sea Level Change. In
1174 Climate Change 2021: The Physical Science Basis. Contribution of Working Group I to
1175 the Sixth Assessment Report of the Intergovernmental Panel on Climate Change.
1176 Cambridge University Press, Cambridge, United Kingdom and New York, NY, USA
- 1177 Fuchs V, Teixeira GLG, Nzualo T das NM (2021) Estimation of nautical chart datum by the
1178 statistical method in micro and meso tidal regime: an alternative to the Balay harmonic
1179 method. *Int Hydrogr Rev* 26:
- 1180 Gaffet A, Bertin X, Sous D, et al (2024) A new global high resolution wave model for the
1181 tropical ocean. *EGUSphere Prepr.* <https://doi.org/10.5194/egusphere-2024-2610>
- 1182 Green J, Haigh ID, Quinn N, et al (2025) Review article: A comprehensive review of compound
1183 flooding literature with a focus on coastal and estuarine regions. *Nat Hazards Earth Syst*
1184 *Sci* 25:747–816. <https://doi.org/10.5194/nhess-25-747-2025>
- 1185 Guérin T, Bertin X, Coulombier T, de Bakker A (2018) Impacts of wave-induced circulation
1186 in the surf zone on wave setup. *Ocean Model* 123:86–97.
1187 <https://doi.org/10.1016/j.ocemod.2018.01.006>
- 1188 Hallegatte S, Green C, Nicholls RJ, Corfee-Morlot J (2013) Future flood losses in major coastal
1189 cities. *Nat Clim Change* 3:802–806. <https://doi.org/10.1038/nclimate1979>
- 1190 Halverson JB (2018) The costliest hurricane season in U.S. history. *Weatherwise* 71:20–27.
1191 <https://doi.org/10.1080/00431672.2018.1416862>
- 1192 Harrigan S, Zsoter E, Alfieri L, et al (2020) GloFAS-ERA5 operational global river discharge
1193 reanalysis 1979–present. *Earth Syst Sci Data* 12:2043–2060.
1194 <https://doi.org/10.5194/essd-12-2043-2020>

- 1195 Hasselmann K, Barnett T, Bouws E, et al (1973) Measurements of wind-wave growth and swell
1196 decay during the Joint North Sea Wave Project (JONSWAP). *Ergänzungsheft* 8-12
- 1197 Hasselmann S, Hasselmann K, Allender JH, Barnett TP (1985) Computations and
1198 parameterizations of the nonlinear energy transfer in a gravity-wave spectrum. Part II:
1199 parameterizations of the nonlinear energy transfer for application in wave models. *J Phys*
1200 *Oceanogr* 15:1378–1391. [https://doi.org/10.1175/1520-](https://doi.org/10.1175/1520-0485(1985)015<1378:capotn>2.0.co;2)
1201 [0485\(1985\)015<1378:capotn>2.0.co;2](https://doi.org/10.1175/1520-0485(1985)015<1378:capotn>2.0.co;2)
- 1202 Hawker L, Neal J, Savage J, et al (2024) Assessing LISFLOOD-FP with the next-generation
1203 digital elevation model FABDEM using household survey and remote sensing data in the
1204 Central Highlands of Vietnam. *Nat Hazards Earth Syst Sci* 24:539–566.
1205 <https://doi.org/10.5194/nhess-24-539-2024>
- 1206 Hawker L, Uhe P, Paulo L, et al (2022) A 30 m global map of elevation with forests and
1207 buildings removed. *Environ Res Lett* 17:024016. [https://doi.org/10.1088/1748-](https://doi.org/10.1088/1748-9326/ac4d4f)
1208 [9326/ac4d4f](https://doi.org/10.1088/1748-9326/ac4d4f)
- 1209 Hersbach H, Bell B, Berrisford P, et al (2018) ERA5 hourly data on single levels from 1940 to
1210 present
- 1211 Hersbach H, Bell B, Berrisford P, et al (2020) The ERA5 global reanalysis. *Q J R Meteorol*
1212 *Soc* 146:1999–2049. <https://doi.org/10.1002/qj.3803>
- 1213 Holland GJ (1980) An analytic model of the wind and pressure profiles in hurricanes. *Mon*
1214 *Weather Rev* 108:1212–1218. [https://doi.org/10.1175/1520-](https://doi.org/10.1175/1520-0493(1980)108<1212:aamotw>2.0.co;2)
1215 [0493\(1980\)108<1212:aamotw>2.0.co;2](https://doi.org/10.1175/1520-0493(1980)108<1212:aamotw>2.0.co;2)
- 1216 Huang W, Ye F, Zhang YJ, et al (2021) Compounding factors for extreme flooding around
1217 Galveston Bay during Hurricane Harvey. *Ocean Model* 158:101735.
1218 <https://doi.org/10.1016/j.ocemod.2020.101735>

- 1219 Huang W, Zhang YJ, Liu Z, et al (2023) Simulation of compound flooding in Japan using a
 1220 nationwide model. *Nat Hazards* 117:2693–2713. [https://doi.org/10.1007/s11069-023-](https://doi.org/10.1007/s11069-023-05962-7)
 1221 05962-7
- 1222 Huang W, Zhang YJ, Wang Z, et al (2022) Tidal simulation revisited. *Ocean Dyn.*
 1223 <https://doi.org/10.1007/s10236-022-01498-9>
- 1224 Idier D, Dumas F, Muller H (2012) Tide-surge interaction in the English Channel. *Nat Hazards*
 1225 *Earth Syst Sci* 12:3709–3718. <https://doi.org/10.5194/nhess-12-3709-2012>
- 1226 IMF (2023) World Economic Outlook database.
 1227 [https://www.imf.org/en/Publications/WEO/weo-database/2023/October/weo-](https://www.imf.org/en/Publications/WEO/weo-database/2023/October/weo-report?c=674,&s=NGDPD,PPPGDP,NGDPDPC,PPPPC,&sy=2020&ey=2028&ssm=0&scsm=1&scc=0&ssd=1&ssc=0&sic=0&sort=country&ds=.&br=1)
 1228 [report?c=674,&s=NGDPD,PPPGDP,NGDPDPC,PPPPC,&sy=2020&ey=2028&ssm=0](https://www.imf.org/en/Publications/WEO/weo-database/2023/October/weo-report?c=674,&s=NGDPD,PPPGDP,NGDPDPC,PPPPC,&sy=2020&ey=2028&ssm=0&scsm=1&scc=0&ssd=1&ssc=0&sic=0&sort=country&ds=.&br=1)
 1229 [&scsm=1&scc=0&ssd=1&ssc=0&sic=0&sort=country&ds=.&br=1](https://www.imf.org/en/Publications/WEO/weo-database/2023/October/weo-report?c=674,&s=NGDPD,PPPGDP,NGDPDPC,PPPPC,&sy=2020&ey=2028&ssm=0&scsm=1&scc=0&ssd=1&ssc=0&sic=0&sort=country&ds=.&br=1). Accessed 13 Dec
 1230 2024
- 1231 Jaafar HH, Ahmad FA, El Beyrouthy N (2019) GCN250, new global gridded curve numbers
 1232 for hydrologic modeling and design. *Sci Data* 6:. [https://doi.org/10.1038/s41597-019-](https://doi.org/10.1038/s41597-019-0155-x)
 1233 0155-x
- 1234 Kennedy AB, Wirasaet D, Begmohammadi A, et al (2019) Subgrid theory for storm surge
 1235 modeling. *Ocean Model* 144:101491. <https://doi.org/10.1016/j.ocemod.2019.101491>
- 1236 Khan MJU, Ansary MN, Durand F, et al (2019) High-resolution intertidal topography from
 1237 Sentinel-2 multi-spectral imagery: synergy between remote sensing and numerical
 1238 modeling. *Remote Sens* 11:2888. <https://doi.org/10.3390/rs11242888>
- 1239 Khan MJU, Durand F, Bertin X, et al (2021) Towards an efficient storm surge and inundation
 1240 forecasting system over the Bengal delta: chasing the Supercyclone Amphan. *Nat*
 1241 *Hazards Earth Syst Sci* 21:2523–2541. <https://doi.org/10.5194/nhess-21-2523-2021>

- 1242 Khan MJU, Durand F, Emanuel K, et al (2022) Storm surge hazard over Bengal delta: a
1243 probabilistic–deterministic modelling approach. Nat Hazards Earth Syst Sci 22:2359–
1244 2379. <https://doi.org/10.5194/nhess-22-2359-2022>
- 1245 Khan MJU, Durand F, Testut L, et al (2020) Sea level rise inducing tidal modulation along the
1246 coasts of Bengal delta. Cont Shelf Res 211:104289.
1247 <https://doi.org/10.1016/j.csr.2020.104289>
- 1248 Kitambo B, Papa F, Paris A, et al (2022) A combined use of in situ and satellite-derived
1249 observations to characterize surface hydrology and its variability in the Congo River
1250 Basin. Hydrol Earth Syst Sci 26:1857–1882. <https://doi.org/10.5194/hess-26-1857-2022>
- 1251 Knapp KR, Diamond HJ, Kossin JP, et al (2018) International Best Track Archive for Climate
1252 Stewardship (IBTrACS) project, version 4
- 1253 Knutson T, Camargo SJ, Chan JCL, et al (2020) Tropical cyclones and climate change
1254 assessment: Part II: projected response to anthropogenic warming. Bull Am Meteorol
1255 Soc 101:E303–E322. <https://doi.org/10.1175/BAMS-D-18-0194.1>
- 1256 Krien Y, Arnaud G, Cécé R, et al (2018) Can we improve parametric cyclonic wind fields using
1257 recent satellite remote sensing data? Remote Sens 10:1963.
1258 <https://doi.org/10.3390/rs10121963>
- 1259 Krien Y, Dudon B, Roger J, et al (2017a) Assessing storm surge hazard and impact of sea level
1260 rise in the Lesser Antilles case study of Martinique. Nat Hazards Earth Syst Sci 17:1559–
1261 1571. <https://doi.org/10.5194/nhess-17-1559-2017>
- 1262 Krien Y, Mayet C, Testut L, et al (2016) Improved bathymetric dataset and tidal model for the
1263 northern Bay of Bengal. Mar Geod 39:422–438.
1264 <https://doi.org/10.1080/01490419.2016.1227405>

- 1265 Krien Y, Testut L, Islam AKMS, et al (2017b) Towards improved storm surge models in the
1266 northern Bay of Bengal. Cont Shelf Res 135:58–73.
1267 <https://doi.org/10.1016/j.csr.2017.01.014>
- 1268 Kumar P, Srivastava SS, Jivani N, et al (2024) Long-term assessment of ERA5 reanalysis
1269 rainfall for lightning events over India observed by Tropical Rainfall Measurement
1270 Mission Lightning Imaging Sensor. Q J R Meteorol Soc 150:2472–2488.
1271 <https://doi.org/10.1002/qj.4719>
- 1272 Le Quotidien (2022) Batsirai : 47 millions de pertes agricoles.
1273 [https://www.lequotidien.re/actualites/economie/batsirai-47-millions-de-pertes-](https://www.lequotidien.re/actualites/economie/batsirai-47-millions-de-pertes-agricoles/)
1274 [agricoles/](https://www.lequotidien.re/actualites/economie/batsirai-47-millions-de-pertes-agricoles/). Accessed 28 Nov 2024
- 1275 Lehner B, Grill G (2013) Global river hydrography and network routing: baseline data and new
1276 approaches to study the world’s large river systems. Hydrol Process 27:2171–2186.
1277 <https://doi.org/10.1002/hyp.9740>
- 1278 Leijnse T, van Ormondt M, Nederhoff K, van Dongeren A (2021) Modeling compound
1279 flooding in coastal systems using a computationally efficient reduced-physics solver:
1280 Including fluvial, pluvial, tidal, wind- and wave-driven processes. Coast Eng
1281 163:103796. <https://doi.org/10.1016/j.coastaleng.2020.103796>
- 1282 Leroux M-D, Amélie V, Bonnardot F, et al (2023) Régionalisation du changement climatique
1283 et développement de services climatiques dans le sud-ouest de l’océan Indien et ses
1284 territoires insulaires. METEO FRANCE
- 1285 Leroux M-D, Bonnardot F, Somot S, et al (2024) Developing climate services for vulnerable
1286 islands in the Southwest Indian Ocean: A combined statistical and dynamical CMIP6
1287 downscaling approach for climate change assessment. Clim Serv 34:100491.
1288 <https://doi.org/10.1016/j.cliser.2024.100491>

- 1289 Li W, Li D, Fang ZN (2023) Intercomparison of automated near-real-time flood mapping
 1290 algorithms using satellite data and DEM-based methods: a case study of 2022
 1291 Madagascar flood. *Hydrology* 10:17. <https://doi.org/10.3390/hydrology10010017>
- 1292 Lin N, Chavas D (2012) On hurricane parametric wind and applications in storm surge
 1293 modeling. *J Geophys Res Atmospheres* 117:n/a-n/a.
 1294 <https://doi.org/10.1029/2011jd017126>
- 1295 Lin N, Emanuel K, Oppenheimer M, Vanmarcke E (2012) Physically based assessment of
 1296 hurricane surge threat under climate change. *Nat Clim Change* 2:462–467.
 1297 <https://doi.org/10.1038/nclimate1389>
- 1298 Lin P, Pan M, Beck HE, et al (2019) Global reconstruction of naturalized river flows at 2.94
 1299 million reaches. *Water Resour Res* 55:6499–6516.
 1300 <https://doi.org/10.1029/2019wr025287>
- 1301 Liu Z, Wang H, Zhang YJ, et al (2020) Cross-scale modeling of storm surge, tide, and
 1302 inundation in Mid-Atlantic Bight and New York City during Hurricane Sandy, 2012.
 1303 *Estuar Coast Shelf Sci* 233:106544. <https://doi.org/10.1016/j.ecss.2019.106544>
- 1304 Lyard FH, Allain DJ, Cancet M, et al (2021) FES2014 global ocean tide atlas: design and
 1305 performance. *Ocean Sci* 17:615–649. <https://doi.org/10.5194/os-17-615-2021>
- 1306 Martins K, Bertin X, Mengual B, et al (2022) Wave-induced mean currents and setup over
 1307 barred and steep sandy beaches. *Ocean Model* 179:102110.
 1308 <https://doi.org/10.1016/j.ocemod.2022.102110>
- 1309 Mason DC, Gurney C, Kennett M (2000) Beach topography mapping—a comparison of
 1310 techniques. *J Coast Conserv* 6:113–124. <https://doi.org/10.1007/bf02730475>
- 1311 Mazza E, Chen SS (2023) Tropical cyclone rainfall climatology, extremes, and flooding
 1312 potential from remote sensing and reanalysis datasets over the continental United States.
 1313 *J Hydrometeorol* 24:1549–1562. <https://doi.org/10.1175/jhm-d-22-0199.1>

- 1314 Mentaschi L, Vousdoukas MI, García-Sánchez G, et al (2023) A global unstructured, coupled,
1315 high-resolution hindcast of waves and storm surge. *Front Mar Sci* 10:.
1316 <https://doi.org/10.3389/fmars.2023.1233679>
- 1317 Mishra SK, Singh VP (2003) Soil Conservation Service Curve Number (SCS-CN)
1318 methodology. Springer Netherlands
- 1319 Muis S, Apecechea MI, Dullaart J, et al (2020) A high-resolution global dataset of extreme sea
1320 levels, tides, and storm surges, including future projections. *Front Mar Sci* 7:.
1321 <https://doi.org/10.3389/fmars.2020.00263>
- 1322 Mulet S, Rio M-H, Etienne H, et al (2021) The new CNES-CLS18 global mean dynamic
1323 topography. *Ocean Sci* 17:789–808. <https://doi.org/10.5194/os-17-789-2021>
- 1324 Nash DJ, Pribyl K, Klein J, et al (2014) Tropical cyclone activity over Madagascar during the
1325 late nineteenth century. *Int J Climatol* 35:3249–3261. <https://doi.org/10.1002/joc.4204>
- 1326 Nederhoff K, Leijnse TWB, Parker K, et al (2024) Tropical or extratropical cyclones: what
1327 drives the compound flood hazard, impact, and risk for the United States Southeast
1328 Atlantic coast? *Nat Hazards* 120:8779–8825. [https://doi.org/10.1007/s11069-024-06552-](https://doi.org/10.1007/s11069-024-06552-x)
1329 [x](https://doi.org/10.1007/s11069-024-06552-x)
- 1330 Needham HF, Keim BD, Sathiaraj D (2015) A review of tropical cyclone-generated storm
1331 surges: global data sources, observations, and impacts. *Rev Geophys* 53:545–591.
1332 <https://doi.org/10.1002/2014rg000477>
- 1333 Normandin C, Frappart F, Diepkilé AT, et al (2018) Evolution of the performances of radar
1334 altimetry missions from ERS-2 to Sentinel-3A over the Inner Niger Delta. *Remote Sens*
1335 10:833. <https://doi.org/10.3390/rs10060833>
- 1336 OCHA (2022a) Southern Africa: Cyclone season flash update no. 3 (Tropical Cyclone Batsirai)
1337 (7 February 2022). [https://reliefweb.int/report/madagascar/southern-africa-cyclone-](https://reliefweb.int/report/madagascar/southern-africa-cyclone-season-flash-update-no-3-tropical-cyclone-batsirai-7)
1338 [season-flash-update-no-3-tropical-cyclone-batsirai-7](https://reliefweb.int/report/madagascar/southern-africa-cyclone-season-flash-update-no-3-tropical-cyclone-batsirai-7). Accessed 13 Nov 2024

- 1339 OCHA (2022b) Southern Africa: Cyclone season flash update no. 6 (Tropical Cyclone Batsirai)
 1340 (13 February 2022). [https://reliefweb.int/report/madagascar/southern-africa-cyclone-](https://reliefweb.int/report/madagascar/southern-africa-cyclone-season-flash-update-no-6-tropical-cyclone-batsirai-13)
 1341 [season-flash-update-no-6-tropical-cyclone-batsirai-13](https://reliefweb.int/report/madagascar/southern-africa-cyclone-season-flash-update-no-6-tropical-cyclone-batsirai-13). Accessed 13 Nov 2024
- 1342 OCHA (2022c) Madagascar: Rainy and cyclone season flash update no.1 (24 January 2022).
 1343 [https://reliefweb.int/report/madagascar/madagascar-rainy-and-cyclone-season-flash-](https://reliefweb.int/report/madagascar/madagascar-rainy-and-cyclone-season-flash-update-no1-24-january-2022)
 1344 [update-no1-24-january-2022](https://reliefweb.int/report/madagascar/madagascar-rainy-and-cyclone-season-flash-update-no1-24-january-2022). Accessed 9 Dec 2024
- 1345 OCHA (2022d) Southern Africa: Cyclone season flash update no. 10 (2 March 2022).
 1346 [https://reliefweb.int/report/madagascar/southern-africa-cyclone-season-flash-update-no-](https://reliefweb.int/report/madagascar/southern-africa-cyclone-season-flash-update-no-10-2-march-2022)
 1347 [10-2-march-2022](https://reliefweb.int/report/madagascar/southern-africa-cyclone-season-flash-update-no-10-2-march-2022). Accessed 9 Dec 2024
- 1348 Olcese G, Bates PD, Neal JC, et al (2024) Developing a fluvial and pluvial stochastic flood
 1349 model of Southeast Asia. *Water Resour Res* 60:. <https://doi.org/10.1029/2023wr036580>
- 1350 Paul BK (2009) Why relatively fewer people died? The case of Bangladesh's Cyclone Sidr.
 1351 *Nat Hazards* 50:289–304. <https://doi.org/10.1007/s11069-008-9340-5>
- 1352 Pekel J-F, Cottam A, Gorelick N, Belward AS (2016) High-resolution mapping of global
 1353 surface water and its long-term changes. *Nature* 540:418–422.
 1354 <https://doi.org/10.1038/nature20584>
- 1355 Pezerat M, Bertin X, Martins K, et al (2021) Simulating storm waves in the nearshore area
 1356 using spectral model: current issues and a pragmatic solution. *Ocean Model* 158:101737.
 1357 <https://doi.org/10.1016/j.ocemod.2020.101737>
- 1358 Pfahl S, O’Gorman PA, Fischer EM (2017) Understanding the regional pattern of projected
 1359 future changes in extreme precipitation. *Nat Clim Change* 7:423–427.
 1360 <https://doi.org/10.1038/nclimate3287>
- 1361 Pickering MD, Horsburgh KJ, Blundell JR, et al (2017) The impact of future sea-level rise on
 1362 the global tides. *Cont Shelf Res* 142:50–68. <https://doi.org/10.1016/j.csr.2017.02.004>

- 1363 Ponce VM, Hawkins RH (1996) Runoff Curve Number: has it reached maturity? J Hydrol Eng
1364 1:11–19. [https://doi.org/10.1061/\(asce\)1084-0699\(1996\)1:1\(11\)](https://doi.org/10.1061/(asce)1084-0699(1996)1:1(11))
- 1365 Prime T (2018) Relocatable tide prediction and storm surge forecasting. In: Volume 7B: Ocean
1366 Engineering. American Society of Mechanical Engineers
- 1367 Ramsay HA, Camargo SJ, Kim D (2011) Cluster analysis of tropical cyclone tracks in the
1368 Southern Hemisphere. Clim Dyn 39:897–917. [https://doi.org/10.1007/s00382-011-1225-](https://doi.org/10.1007/s00382-011-1225-8)
1369 8
- 1370 Reguero BG, Menéndez M, Méndez FJ, et al (2012) A Global Ocean Wave (GOW) calibrated
1371 reanalysis from 1948 onwards. Coast Eng 65:38–55.
1372 <https://doi.org/10.1016/j.coastaleng.2012.03.003>
- 1373 Reuters (2022) Madagascar cyclone kills 21, leaves homes and lives in ruins.
1374 [https://www.reuters.com/world/africa/hit-by-second-cyclone-two-weeks-madagascar-](https://www.reuters.com/world/africa/hit-by-second-cyclone-two-weeks-madagascar-struggles-bring-relief-2022-02-07/)
1375 [struggles-bring-relief-2022-02-07/](https://www.reuters.com/world/africa/hit-by-second-cyclone-two-weeks-madagascar-struggles-bring-relief-2022-02-07/). Accessed 13 Nov 2024
- 1376 Rija F (2019) Renforcement du Service d’Information Climatique MAPROOM de Madagascar
1377 pour répondre aux besoins des secteurs clés de développement. Meteo Madagascar,
1378 Antananarivo
- 1379 Roland A, Zhang YJ, Wang HV, et al (2012) A fully coupled 3D wave-current interaction
1380 model on unstructured grids. J Geophys Res Oceans 117:n/a-n/a.
1381 <https://doi.org/10.1029/2012jc007952>
- 1382 Rossman LA, Huber WC (2016) Storm Water Management Model reference manual volume I
1383 – Hydrology, January 2016. US Environmental Protection Agency
- 1384 Santos da Silva J, Calmant S, Seyler F, et al (2010) Water levels in the Amazon basin derived
1385 from the ERS 2 and ENVISAT radar altimetry missions. Remote Sens Environ
1386 114:2160–2181. <https://doi.org/10.1016/j.rse.2010.04.020>

- 1387 Seeger K, Minderhoud PSJ, Peffeköver A, et al (2023) Assessing land elevation in the
1388 Ayeyarwady Delta (Myanmar) and its relevance for studying sea level rise and delta
1389 flooding. *Hydrol Earth Syst Sci* 27:2257–2281. [https://doi.org/10.5194/hess-27-2257-](https://doi.org/10.5194/hess-27-2257-2023)
1390 2023
- 1391 Simon B (2013) Coastal tides. Institut océanographie éd.
- 1392 Stockdon HF, Holman RA, Howd PA, Sallenger AH (2006) Empirical parameterization of
1393 setup, swash, and runup. *Coast Eng* 53:573–588.
1394 <https://doi.org/10.1016/j.coastaleng.2005.12.005>
- 1395 Sun W, Ishidaira H, Bastola S (2012) Calibration of hydrological models in ungauged basins
1396 based on satellite radar altimetry observations of river water level. *Hydrol Process*
1397 26:3524–3537. <https://doi.org/10.1002/hyp.8429>
- 1398 Suzzi-Simmons A (2023) Status of deforestation of Madagascar. *Glob Ecol Conserv*
1399 42:e02389. <https://doi.org/10.1016/j.gecco.2023.e02389>
- 1400 Szabó AI, Raveloson A, Székely B (2015) Landscape evolution and climate in Madagascar:
1401 lavakization in the light of archive precipitation data. *Cuad Investig Geográfica* 41:181–
1402 204. <https://doi.org/10.18172/cig.2646>
- 1403 Thackeray CW, Hall A, Norris J, Chen D (2022) Constraining the increased frequency of global
1404 precipitation extremes under warming. *Nat Clim Change* 12:441–448.
1405 <https://doi.org/10.1038/s41558-022-01329-1>
- 1406 Tran HQ, Ayala Cruz F, McCarroll J, Babanin A (2024) Non-linear surges and extreme wind-
1407 waves in Port Phillip Bay under existing and future mean sea levels. *Front Mar Sci*
1408 11:1480054. <https://doi.org/10.3389/fmars.2024.1480054>
- 1409 Van Ormondt M, Leijnse T, De Goede R, et al (2025) Subgrid corrections for the linear inertial
1410 equations of a compound flood model – a case study using SFINCS 2.1.1 Dollerup
1411 release. *Geosci Model Dev* 18:843–861. <https://doi.org/10.5194/gmd-18-843-2025>

- 1412 Vecchi GA, Knutson TR (2011) Estimating annual numbers of Atlantic hurricanes missing
1413 from the HURDAT Database (1878–1965) using ship track density. *J Clim* 24:1736–
1414 1746. <https://doi.org/10.1175/2010jcli3810.1>
- 1415 Vieilledent G, Grinand C, Rakotomalala FA, et al (2018) Combining global tree cover loss data
1416 with historical national forest cover maps to look at six decades of deforestation and
1417 forest fragmentation in Madagascar. *Biol Conserv* 222:189–197.
1418 <https://doi.org/10.1016/j.biocon.2018.04.008>
- 1419 Vitousek S, Barnard PL, Fletcher CH, et al (2017) Doubling of coastal flooding frequency
1420 within decades due to sea-level rise. *Sci Rep* 7:. [https://doi.org/10.1038/s41598-017-](https://doi.org/10.1038/s41598-017-01362-7)
1421 [01362-7](https://doi.org/10.1038/s41598-017-01362-7)
- 1422 Wahl T, Jain S, Bender J, et al (2015) Increasing risk of compound flooding from storm surge
1423 and rainfall for major US cities. *Nat Clim Change* 5:1093–1097.
1424 <https://doi.org/10.1038/nclimate2736>
- 1425 Webster PJ (2008) Myanmar’s deadly daffodil. *Nat Geosci* 1:488–490.
1426 <https://doi.org/10.1038/ngeo257>
- 1427 Welker C, Faust E (2013) Tropical cyclone-related socio-economic losses in the Western North
1428 Pacific region. *Nat Hazards Earth Syst Sci* 13:115–124. [https://doi.org/10.5194/nhess-](https://doi.org/10.5194/nhess-13-115-2013)
1429 [13-115-2013](https://doi.org/10.5194/nhess-13-115-2013)
- 1430 Wing OEJ, Bates PD, Quinn ND, et al (2024) A 30 m global flood inundation model for any
1431 climate scenario. *Water Resour Res* 60:. <https://doi.org/10.1029/2023wr036460>
- 1432 WMO (2022) Cyclone Batsirai hits Madagascar. [https://wmo.int/media/news/cyclone-batsirai-](https://wmo.int/media/news/cyclone-batsirai-hits-madagascar)
1433 [hits-madagascar](https://wmo.int/media/news/cyclone-batsirai-hits-madagascar). Accessed 13 Nov 2024
- 1434 WW3DG TWIDG (2019) User manual and system documentation of WAVEWATCH III TM

- 1435 Xu K, Wang C, Bin L (2022) Compound flood models in coastal areas: a review of methods
1436 and uncertainty analysis. *Nat Hazards* 116:469–496. [https://doi.org/10.1007/s11069-](https://doi.org/10.1007/s11069-022-05683-3)
1437 022-05683-3
- 1438 Zhang Y, Baptista AM (2008) SELFE: A semi-implicit Eulerian–Lagrangian finite-element
1439 model for cross-scale ocean circulation. *Ocean Model* 21:71–96.
1440 <https://doi.org/10.1016/j.ocemod.2007.11.005>
- 1441 Zhang Y, Schaap MG (2019) Estimation of saturated hydraulic conductivity with pedotransfer
1442 functions: A review. *J Hydrol* 575:1011–1030.
1443 <https://doi.org/10.1016/j.jhydrol.2019.05.058>
- 1444 Zhang Y, Schaap MG, Wei Z (2020a) Development of hierarchical ensemble model and
1445 estimates of soil water retention with global coverage. *Geophys Res Lett* 47:..
1446 <https://doi.org/10.1029/2020gl088819>
- 1447 Zhang YJ, Fernandez-Montblanc T, Pringle W, et al (2023) Global seamless tidal simulation
1448 using a 3D unstructured-grid model (SCHISM v5.10.0). *Geosci Model Dev* 16:2565–
1449 2581. <https://doi.org/10.5194/gmd-16-2565-2023>
- 1450 Zhang YJ, Ye F, Stanev EV, Grashorn S (2016) Seamless cross-scale modeling with SCHISM.
1451 *Ocean Model* 102:64–81. <https://doi.org/10.1016/j.ocemod.2016.05.002>
- 1452 Zhang YJ, Ye F, Yu H, et al (2020b) Simulating compound flooding events in a hurricane.
1453 *Ocean Dyn*. <https://doi.org/10.1007/s10236-020-01351-x>

1454

1455

Statements and Declarations

Funding

This work was supported by the Belmont Forum Collaborative Research Action Migration 2022 funding window. Through the Belmont initiative, this work would not have been possible without the financial support of the Agence Nationale de la Recherche (Grant ANR-22-MIGR-0001-01) and the National Science Foundation (#2318924). This project was provided with HPC and storage resources by GENCI at TGCC thanks to the grant 2024-A0170107298 on the supercomputer Joliot Curie's SKL partition.

Competing interests

The authors have no relevant financial or non-financial competing interests to disclose.

Author contributions

Md Jamal Uddin Khan and Fabien Durand designed the study. SFINCS model configuration was developed by Md Jamal Uddin Khan, SCHISM-WWM model configuration was developed by M. Afroosa and Md Jamal Uddin Khan, and WW3 model was developed by Xavier Bertin. All simulations, and analysis presented in the manuscript were done by Md Jamal Uddin Khan. The first draft of the manuscript was written by Md Jamal Uddin Khan and all authors commented on previous versions of the manuscript. All authors read and approved the final manuscript.